³Impacts of CP and EP El Niño Events on the Antarctic Sea Ice in Austral Spring

Chao Zhang, a Tim Li, b,c and Shuanglin Lia,d,e

^a Department of Atmospheric Science, School of Environmental Studies, China University of Geosciences, Wuhan, China
^b International Pacific Research Center and Department of Atmospheric Sciences, School of Ocean and Earth Science and
Technology, University of Hawai'i at Mānoa, Honolulu, Hawaii

^c Key Laboratory of Meteorological Disaster, Ministry of Education (KLME)/Joint International Research Laboratory of Climate and Environmental Change (ILCEC)/Collaborative Innovation Center on Forecast and Evaluation of Meteorological Disasters (CIC FEMD), Nanjing University of Information Science and Technology, Nanjing, China

^d Institute of Atmospheric Physics/Climate Change Research Center, Chinese Academy of Sciences, Beijing, China ^e College of Earth and Planetary Sciences, University of the Chinese Academy of Sciences, Beijing, China

(Manuscript received 6 January 2021, in final form 9 July 2021)

ABSTRACT: Based on observational data analyses and idealized modeling experiments, we investigated the distinctive impacts of central Pacific (CP) El Niño and eastern Pacific (EP) El Niño on the Antarctic sea ice concentration (SIC) in austral spring (September–November). The tropical heat sources associated with EP El Niño and the co-occurring positive phase of the Indian Ocean dipole (IOD) excite two branches of Rossby wave trains that propagate southeastward, causing an anomalous anticyclone over the eastern Ross–Amundsen–Bellingshausen Seas. Anomalous northerly (southerly) wind to the west (east) of the anomalous anticyclone favors poleward (offshore) movements of sea ice, resulting in a sea ice loss (growth) in the eastern Ross–Amundsen Seas (the Bellingshausen–Weddell Seas). Meanwhile, the anomalous northerly (southerly) wind also advects warmer and wetter (colder and drier) air into the eastern Ross–Amundsen Seas (the Bellingshausen–Weddell Seas), causing surface warming (cooling) through the enhanced (reduced) surface heat fluxes and thus contributing to the sea ice melting (growth). CP El Niño, however, forces a Rossby wave train that generates an anomalous anticyclone in the eastern Ross–Amundsen Seas, 20° west of that caused by EP El Niño. Consequently, a positive SIC anomaly occurs in the Bellingshausen Sea. A dry version of the Princeton atmospheric general circulation model was applied to verify the roles of anomalous heating in the tropics. The result showed that EP El Niño can remotely induce an anomalous anticyclone and associated dipole temperature pattern in the Antarctic region, whereas CP El Niño generates a similar anticyclone pattern with its location shift westward by 20° in longitudes.

KEYWORDS: Air-sea interaction; El Nino; ENSO; Sea ice

1. Introduction

Antarctic sea ice is an important component of the climate system in the Southern Hemisphere (e.g., Simmonds and Wu 1993; Hobbs and Raphael 2010), which may act as an early indicator of climate change (Simpkins et al. 2012; Bintanja et al. 2013). It is now well established that significant changes are happening in the Antarctic (e.g., Rintoul et al. 2018; Steig 2019), especially in the West Antarctic where strong sea ice variability occurs (Schneider and Steig 2008; Stammerjohn et al. 2008; Li et al. 2014; Parkinson 2019). For instance, following a slow increase in 1979-2014, the annual mean total extent of Antarctic sea ice decreased rapidly in 2014-18 and reached a record low in 2016 (Parkinson 2019; Purich and England 2019; Wang et al. 2019b). Sea ice decline occurred in most parts of the West Antarctic (Parkinson 2019). Usually, observations show a dipole structure in the sea ice distribution in the West Antarctic, which is known as the Antarctic dipole (ADP) (Yuan and Martinson 2000, 2001). The ADP has a dominant interannual time scale

Openotes content that is immediately available upon publication as open access.

 ${\it Corresponding\ authors:}\ Tim\ Li, timli@hawaii.edu; Shuanglin\ Li, shuanglin.li@mail.iap.ac.cn$

(Harangozo 2000; Liu et al. 2002) and is characterized by a seesaw not only in sea ice but also in surface temperature and sea level pressure anomalies between the Ross–Amundsen Seas and Bellingshausen–Weddell Seas (Yuan and Martinson 2000, 2001; Yuan 2004).

A number of studies have linked the sea ice variability in the ADP region to the Amundsen Sea low (ASL), southern annular mode (SAM), a quasi-stationary wavenumber-3 pattern (ZW3), and a semiannual oscillation (e.g., White and Peterson 1996; Pezza et al. 2012; Clem and Fogt 2015; Turner et al. 2016). However, the effects of El Niño-Southern Oscillation (ENSO) are dominant on the interannual time scale (Turner 2004; Yuan and Li 2008; Scott et al. 2019). Up to 34% of the variance of the 13-month Gaussian filtered sea ice extent in the West Antarctic can be explained by ENSO (Yuan and Martinson 2000). Several studies have shown that sea ice changes in the Ross and Weddell Seas lag the tropical Pacific variability by several months (e.g., Carleton 1989; Simmonds and Jacka 1995). Later work suggested that the relationships with ENSO are concentrated in the regions around the West Antarctic, such as the Ross, Amundsen, Bellingshausen, and Weddell Seas, and projected onto the ADP pattern (Renwick 2002; Hobbs and Raphael 2010; Welhouse et al. 2016). The largest response of sea ice to ENSO is located in the Amundsen Sea (Yuan and Martinson 2000; Renwick 2002).

Several mechanisms have been proposed to explain the links between the sea ice in the West Antarctic and the tropical Pacific

DOI: 10.1175/JCLI-D-21-0002.1

variability. Both Liu et al. (2002) and Yuan (2004) found that the tropical anomalous signals transport to the polar region through an atmospheric bridge, leading to an ADP anomaly during ENSO events. During El Niño, the warm sea surface temperature (SST) in the tropical Pacific enhances the tropical convection and the meridional equator-to-polar thermal gradient in the South Pacific, which strengthens and contracts the Hadley cell (Rind et al. 2001). As a result, the subtropical jet is strengthened and the storm track is shifted equatorward in the South Pacific (Yuan 2004). At the same time, the tropical Pacific warming also results in a descending branch in the tropical Atlantic (Cai et al. 2019), which relaxes and expands the Hadley cell there (Yuan 2004) and then leads to a poleward shift of the storm track in the South Atlantic (Rind et al. 2001). Therefore, changes in the jet streams and the regional Hadley cells apparently enhance the Ferrel cell in the South Pacific and weaken the Ferrel cell in the South Atlantic. As a consequence, more and less heat in the lower latitudes is advected into the Ross-Amundsen Seas and the Bellingshausen-Weddell Seas, respectively, thus contributing to the dipole distribution of sea ice in the West Antarctic (Liu et al. 2002; Yuan 2004). In La Niña condition, the atmospheric circulation is opposite of that in El Niño condition (Yuan 2004).

On the other hand, the sea ice in the West Antarctic also reacts to ENSO through the Pacific–South American (PSA) pattern (Yuan et al. 2018). The PSA is a stationary Rossby wave train triggered by the ENSO-related convection in the western-central tropical Pacific, which propagates southeastward into the West Antarctic (Karoly 1989; Mo 2000). During El Niño, an anomalous anticyclone in association with the upper-tropospheric PSA pattern occurs in the Amundsen-Bellingshausen Seas, which weakens the ASL and results in an anomalous anticyclone (Kreutz et al. 2000; Turner 2004). Northerly wind anomalies to the west of the anomalous anticyclone advect warmer air and SST from lower latitudes to the Ross-Amundsen Seas, leading to a sea ice loss (Liu et al. 2004; Yuan 2004). In contrast, southerly wind anomalies to the east of the anomalous anticyclone tend to advect colder air from the polar region to the Bellingshausen-Weddell Seas, resulting in a sea ice growth.

The ENSO-Antarctic teleconnection studies above considered the ENSO events as a single type. Early in the twenty-first century, El Niño events were classified into two types based on the spatial distribution of SST anomaly, namely the central Pacific (CP) El Niño and eastern Pacific (EP) El Niño types, with the maximum SST anomaly typically occurring in the central and eastern equatorial Pacific, respectively (Ashok et al. 2007a; Yu and Kao 2007; Kug et al. 2009; Yeh et al. 2009). EP El Niño and CP El Niño are quite distinct from each other not only in their onset and developing mechanisms but also in their impacts on the global climate (Kao and Yu 2009; Li et al. 2017; Chen et al. 2019). Typically, EP El Niño begins and develops near the east coast of the tropical Pacific with the maximum SST anomaly in the eastern equatorial Pacific, whereas CP El Niño tends to onset, develop, and decay locally in the central equatorial Pacific (Kao and Yu 2009; Yu et al. 2015). In addition, CP El Niño leads to westward-shifted and localized tropical convection anomalies compared to EP El Niño, resulting in different atmospheric circulation responses in both the Northern and Southern Hemispheres (Feng et al. 2011; Wang et al. 2012; Chung and Li 2013; Sun et al. 2013; Xiang et al. 2013). For example, by using the satellite data, Lee et al. (2010) found that the strong 2009/10 CP El Niño led to a record warming in the south-central Pacific region (35°-55°S, 160°-110°W) and the western Antarctic during austral spring and summer. Song et al. (2011) suggested that the APD persists until austral winter after the peak season of CP El Niño, whereas it does not persist after austral summer after EP El Niño peak. In comparison with EP El Niño, the CP El Niño tends to cause a weaker and northwestward shifting of the PSA pattern, and then leads to a westward shift of ASL and sea ice anomalies in the West Antarctic (Wilson et al. 2014; Ciasto et al. 2015). The above indicates that both CP El Niño and EP El Niño have different impacts on sea ice in the West Antarctic due to the different responses of atmospheric circulation in the Southern Hemisphere (Hurwitz et al. 2011).

In addition to the tropical Pacific variability, the signal in the tropical Indian Ocean, especially the Indian Ocean dipole (IOD) (Saji et al. 1999; Webster et al. 1999), may play active roles in affecting the Antarctic sea ice (e.g., Chan et al. 2008; Meehl et al. 2019; Purich and England 2019; Rondanelli et al. 2019). Extreme IOD events, associated with strong convective diabatic heating in the eastern tropical Indian Ocean that acts as an effective Rossby wave source, can excite a Rossby wave train that propagates southeastward and therefore modulates the surface temperature anomaly in the Southern Hemisphere (Li et al. 2003; Saji et al. 2005; Luo et al. 2010). For instance, the record negative phase of IOD in austral spring 2016 played a key role in contributing to the severity of sea ice decline by the end of 2016 through a Rossby wave train (Wang et al. 2019a). Feng et al. (2019) suggested that the IOD can cause an Antarctic sea ice growth (or loss) through the meridional wind anomalies induced by the IOD-generated atmospheric circulation anomalies.

Generally, the variability in the tropical Indian Ocean and the Pacific are not independent of each other due to their interactions via pan-tropical Walker circulation (e.g., Luo et al. 2012; Cai et al. 2019; Zhang et al. 2019). ENSO and the IOD have repeatedly co-occurred (i.e., El Niño with a positive phase of IOD or La Niña with a negative phase of IOD) in observations since the mid-1970s (Li et al. 2003; Annamalai et al. 2005; Luo et al. 2010), indicating that these two major tropical climate modes might work together to influence the global climate (e.g., Ashok et al. 2004, 2007b). For instance, both Nuncio and Yuan (2015) and Feng et al. (2019) have shown that ENSO and the IOD can work together to influence the Antarctic sea ice. When the IOD occurs alone, its influence on sea ice does not extend to the east of the Amundsen Sea due to the dissipation of the IOD-induced Rossby wave train in the Ross Sea (Nuncio and Yuan 2015; Feng et al. 2019). In comparison, the Rossby wave train can reach to the Bellingshausen Sea, even to the South Atlantic, if ENSO and the IOD coexist (Chan et al. 2008; Cai et al. 2011).

The above studies have advanced further our understanding of the tropics–Antarctic connections. However, the IOD exhibits different features in CP El Niño and EP El Niño. Most of the previous studies only focused on the impacts of the tropical Pacific SST variability associated with the two types of El Niño on the Antarctic sea ice. Whether EP El Niño (or CP El Niño) and the IOD might work together to influence the sea ice is not well documented. Thus, the purpose of this study aims to explore the different impacts of two types of El Niño when each co-occurs with the IOD on the sea ice in the West Antarctic. We mainly focus on austral spring when the impacts of El Niño and IOD on the atmospheric circulation in the Southern Hemisphere are greatest (Jin and Kirtman 2009; Cai et al. 2011).

2. Datasets and methods

a. Datasets

Monthly sea ice concentration (SIC), with a horizontal resolution of $1.0^{\circ} \times 1.0^{\circ}$ and a time span from January 1870 to the present, comes from the Met Office's Hadley Centre (Rayner et al. 2003). Monthly zonal and meridional sea ice velocities are obtained from the European Centre for Medium-Range Weather Forecasts (ECMWF) Ocean Reanalysis System version 5 (ORAS5) (Zuo et al. 2019). The ORAS5 has a horizontal resolution of $1.0^{\circ} \times 1.0^{\circ}$, and covers the period from January 1979 to December 2018. The monthly optimum interpolation SST V2 product with a horizontal resolution of $1.0^{\circ} \times 1.0^{\circ}$ for the period of December 1981–December 2019 is provided by the National Oceanic and Atmospheric Administration (NOAA) (Reynolds et al. 2002). Monthly mean interpolated outgoing longwave radiation (OLR) from June 1974 to the present with a horizontal resolution of 2.5° × 2.5° is obtained from the NOAA (Liebmann and Smith 1996).

Monthly sea level pressure (SLP), air temperature at 2 m, horizontal wind fields at 10 m and at 300 hPa, 300-hPa geopotential height and potential vorticity, surface sensible heat (SH) and latent heat (LH) fluxes, surface net longwave (LW) and shortwave (SW) radiation fluxes, surface specific humidity, and medium and low cloud covers are obtained from the fifthgeneration ECMWF reanalysis (ERA5; C3S 2019). All the variables have horizontal resolutions of 0.25° × 0.25° and time spans from January 1979 to the present. Besides, monthly specific humidity data at 2 m with 2.5° × 2.5° horizontal resolution from the National Centers for Environmental Prediction–National Center for Atmospheric Research (NCEP–NCAR) Reanalysis I through January 1948 to December 2019 are also used (Kalnay et al. 1996).

b. T-N wave activity flux

To examine the Rossby wave pathway, the horizontal wave activity flux or **W** vector formulation, which is derived from the conservation of wave-activity momentum by Takaya and Nakamura (2001), referred to as the T-N wave activity flux, is calculated. The zonal and meridional components of the T-N wave activity flux can be written as

$$W_{x} = \frac{1}{2|\mathbf{U}|} \left\{ \overline{U} \left[\left(\frac{\partial \psi}{\partial x} \right)^{2} - \psi \frac{\partial^{2} \psi}{\partial x^{2}} \right] + \overline{V} \left(\frac{\partial \psi}{\partial x} \frac{\partial \psi}{\partial y} - \psi \frac{\partial^{2} \psi}{\partial x \partial y} \right) \right\}, \tag{1}$$

$$W_{y} = \frac{1}{2|\mathbf{U}|} \left\{ \overline{U} \left(\frac{\partial \psi}{\partial x} \frac{\partial \psi}{\partial y} - \psi \frac{\partial^{2} \psi}{\partial x \partial y} \right) + \overline{V} \left[\left(\frac{\partial \psi}{\partial y} \right)^{2} - \psi \frac{\partial^{2} \psi}{\partial y^{2}} \right] \right\}, \tag{2}$$

where ψ is the geostrophic streamfunction, which is defined as Φ/f (Φ and f are the seasonal mean geopotential height anomaly and Coriolis parameter, respectively); \overline{U} and \overline{V} are the mean zonal and meridional climatological winds, respectively; and $|\mathbf{U}|$ is the magnitude of the mean horizontal winds. Derivatives are computed using centered differences on seasonal anomalies. Here \mathbf{W} vector divergence (convergence) indicates that a Rossby wave is emitted (absorbed)—that is, a wave source (sink) (Takaya and Nakamura 2001; Henderson et al. 2016).

c. Princeton atmospheric general circulation model

To verify the atmospheric circulation responses to the tropical forcing, several numerical experiments are conducted by using a dry version of the Princeton atmospheric general circulation model (AGCM) (Held and Suarez 1994). This AGCM is a primitive equation model based on the sigma $(\sigma = p/p_s)$ coordinate, which was constructed based on the dynamic core of the Geophysical Fluid Dynamic Laboratory AGCM with a horizontal resolution of T42 and five evenly distributed sigma levels ranging from the bottom level at $\sigma =$ 0.9 to the top level at $\sigma = 0.1$ with an interval of 0.2 (Wang et al. 2003; Jiang and Li 2005). No topography is prescribed. In the model, the basic equations include momentum, temperature, and logarithm of surface pressure equations together with the diagnostic equation for the vertical velocity, the detailed expression of which can be found in Jiang and Li (2005).

This anomaly AGCM is linearized by a specified three-dimension seasonal mean basic state, which is similar to the one used by Ting and Yu (1998). Thus, one may examine how the atmosphere responds to a specific anomalous heating in the presence of an idealized or realistic mean state (Wang et al. 2003; Jiang and Li 2005). The perturbation equations retain full nonlinearity and are interpreted as the response to the prescribed forcing. In the present study, a realistic austral spring [September–November (SON)] mean state, which is obtained from the long-term mean of ERA5 is prescribed as the model basic state.

To mimic the planetary boundary layer dissipation, a Rayleigh friction with the damping rate of $1\,\mathrm{day}^{-1}$ at the lowest model level ($\sigma=0.9$) and then linearly decaying to $0.1\,\mathrm{day}^{-1}$ at the level of $\sigma=0.7$ is applied to the momentum equations, while a Newtonian cooling with an e-folding time scale of 15 days is applied to all the model levels in both momentum and heat equations. In addition, the same biharmonic diffusion is applied to the momentum and temperature equations with a dissipating rate of $0.1\,\mathrm{day}^{-1}$ for the smallest resolvable scale in this model. With this dissipation

TABLE 1. Selected cases of EP El Niño and CP El Niño events during 1980–2019. An asterisk (*) means that the El Niño co-occurs with the positive phase of the Indian Ocean dipole (IOD).

EP El Niño	CP El Niño
1982/83*	1994/95*
1991/92*	2002/03
1997/98*	2004/05
2006/07*	2009/10
2015/16*	2014/15
	2018/19*

and diffusion, a steady-state response is realized after about 20 days. The average of the last 20 days of the 40-day integration is used to estimate the steady responses to the tropical heating.

In the study, the analysis period is 40 years from 1980 to 2019. Monthly anomalies are computed relative to the monthly climatology of 1981–2010. We classified CP El Niño and EP El Niño events according to Ren and Jin (2011), that is,

$$\begin{cases} N_{\rm EP} = N_3 - \alpha N_4 \\ N_{\rm CP} = N_4 - \alpha N_3 \end{cases}, \quad \alpha = \begin{cases} 2/5, & N_3 N_4 > 0 \\ 0, & \text{otherwise} \end{cases}$$
 (3)

where N_3 and N_4 denote the Niño-3 and Niño-4 indices—that is, the averaged SST anomalies over the regions 5°N-5°S, 150°-90°W and 5°N-5°S, 170°-120°W, respectively. Based on Eq. (3), six CP El Niño (1994/95, 2002/03, 2004/05, 2009/10, 2014/15, and 2018/19) and five EP El Niño (1982/83, 1991/92, 1997/98, 2006/07, and 2015/16) events are selected during 1980-2019 (Table 1). Note that the 1986-88 El Niño was removed because it started as an EP El Niño but continued as a CP type (Wang et al. 2018). The IOD event is monitored by the dipole mode index (DMI), which is defined as the difference between the averaged SST anomalies over the western (10°N-10°S, 50°-70°E) and eastern (0°-10°S, 90°-110°E) equatorial Indian Ocean (Saji et al. 1999). Additionally, the Southern Ocean around the Antarctic is divided into six sectors: the Ross Sea (160°E–130°W), Amundsen Sea (130°–100°W), Bellingshausen Seas (100°-60°W), Weddell Sea (60°W-20°E), Indian Ocean (20°-90°E), and western Pacific (90°-160°E) based on previous studies (Parkinson and Cavalieri 2012; Parkinson 2019), as shown in Fig. 1.

3. Observed links between the tropics and Antarctic sea ice

Figure 2 shows the composite of seasonal mean SIC anomalies for the five EP El Niño and six CP El Niño events (Table 1). In austral spring (SON) during the developing year of EP El Niño, the distribution of SIC anomalies in the West Antarctic exhibits a dipole pattern, with negative anomalies over the eastern Ross–Amundsen Seas (58°–70°S, 150°–105°W) and positive anomalies over the Bellingshausen–Weddell Seas (55°–70°S, 80°–20°W) (Fig. 2a). In the following austral summer [December to the following February (DJF)] and autumn [March–May (MAM)], no obvious SIC anomalies can be

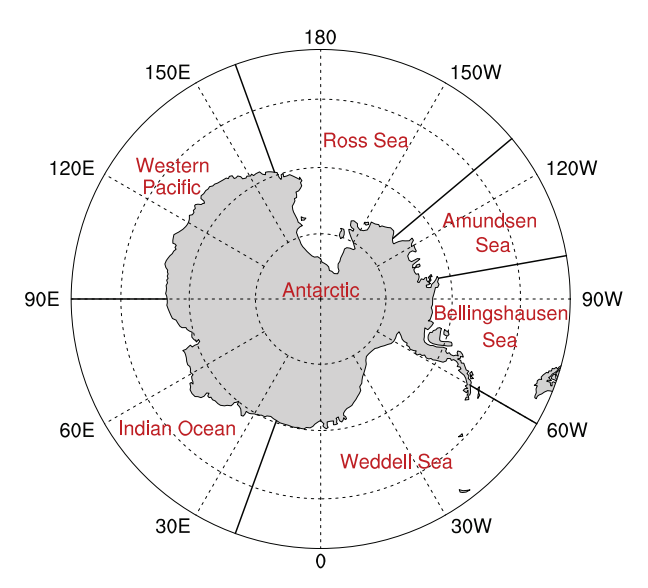


FIG. 1. Identification of six sectors around the Antarctic: Ross Sea (160°E–130°W), Amundsen Sea (130°–100°W), Bellingshausen Sea (100°–60°W), Weddell Sea (60°W–20°E), Indian Ocean (20°–90°E), and western Pacific (90°–160°E).

observed around the Antarctic (Figs. 2b,c). In addition, these SIC anomalies are not statistically significant. In austral winter [June–August (JJA)], the distribution of SIC anomalies in the West Antarctic bears a resemblance to that in austral spring, but only negative SIC anomalies are statistically significant at the 95% confidence level (Fig. 2d).

In comparison, only strong positive SIC anomalies centered in the Bellingshausen Sea (60°-70°S, 105°-55°W) are observed in austral spring during the developing year of CP El Niño (Fig. 2e), which are quite distinct from that of EP type. However, in the following austral summer and autumn, the SIC anomalies have similar spatial structures to that of EP El Niño (Figs. 2f,g). In contrast, the distribution of SIC anomalies in austral winter is quite different from that of EP type (Fig. 2h). Only weak but significant positive SIC anomalies occur in the western Ross Sea, the Bellingshausen Sea, and part of the Weddell Sea. The above indicates that both EP El Niño and CP El Niño have dominant but significant different impacts on the SIC anomalies in the West Antarctic in austral spring compared with the other seasons. In addition, the standard deviations of SIC anomalies in the West Antarctic in austral spring are much higher than the other seasons (Figs. 2i-1). This motivates us to mainly focus on the impacts of the two types of El Niño on the sea ice in austral spring in the present study.

In EP El Niño, the tropical SST anomalies appear as a zonal dipole between the eastern equatorial Pacific and western equatorial Pacific/Maritime Continent (Fig. 3a). Maximum positive SST anomalies typically occur in the central and eastern equatorial Pacific. In addition to the tropical Pacific SST variability, a significant positive phase of IOD can be observed in the equatorial Indian Ocean. Note that all the five selected EP El Niño co-occur with the positive phase of IOD (Table 1). In austral spring, the Niño-3.4 index is significantly

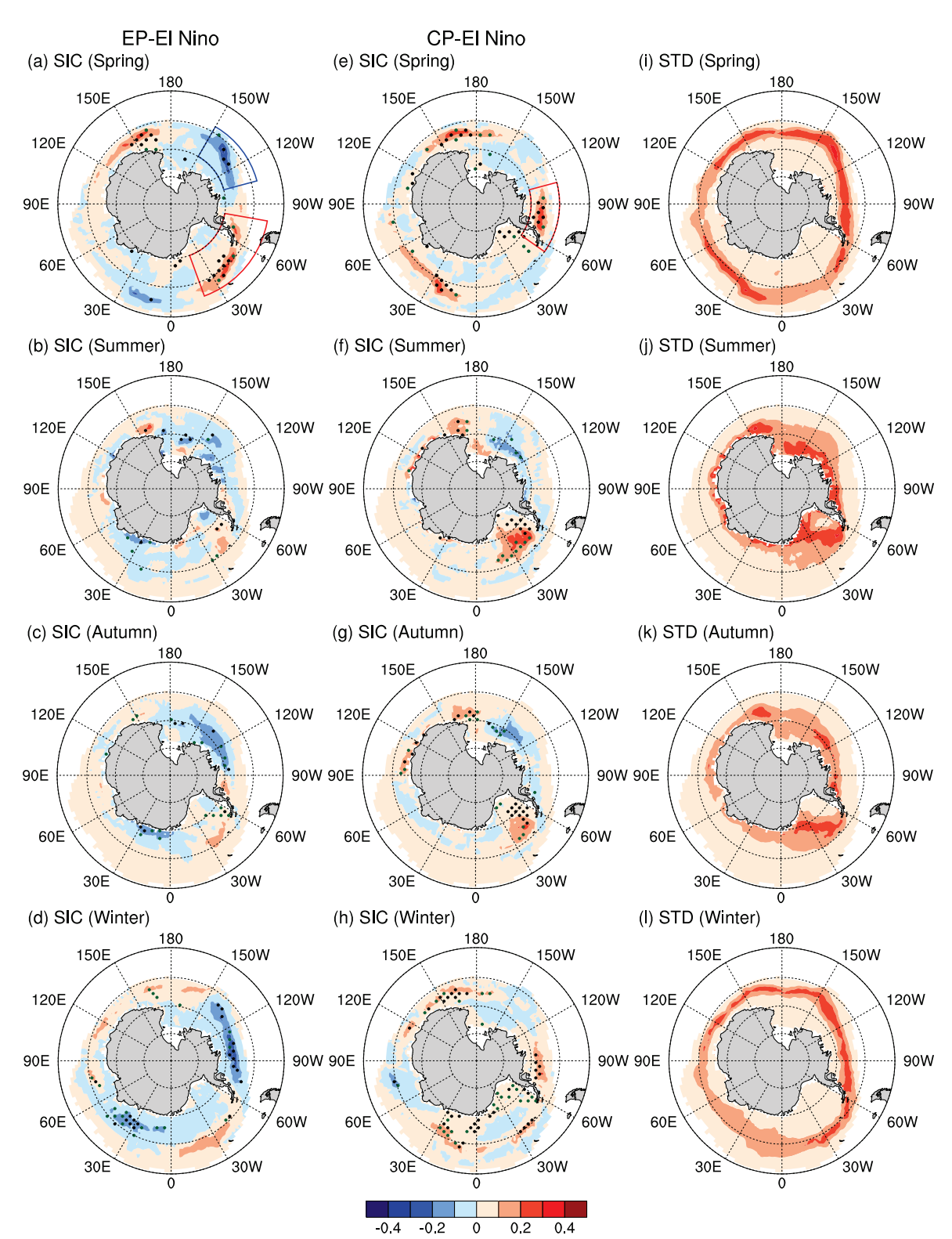


FIG. 2. Composite of sea ice concentration (SIC) anomalies obtained from the Hadley Centre in austral (a),(e) spring (SON), (b),(f) summer (DJF), (c),(g) autumn (MAM), and (d),(h) winter (JJA) for (a)–(d) EP El Niño (1982/83, 1991/92, 1997/98, 2006/07, and 2015/16) and (e)–(h) CP El Niño (1994/95, 2002/03, 2004/05, 2009/10, 2014/15, and 2018/19) events. September–December and January–August are the months in developing and decaying years of El Niño, respectively. (i)–(l) Standard deviations of seasonal mean SIC anomalies calculated based on the period of 1980–2018. The dark green and black stippled areas indicate that the results are statistically significant at the 90% and 95% confidence levels, respectively. The blue $(58^{\circ}-70^{\circ}S, 150^{\circ}-105^{\circ}W)$ and red $(55^{\circ}-70^{\circ}S, 80^{\circ}-20^{\circ}W)$ boxes in (a) and the red box $(60^{\circ}-70^{\circ}S, 105^{\circ}-55^{\circ}W)$ in (e) indicate the sea ice areas that we focus on.

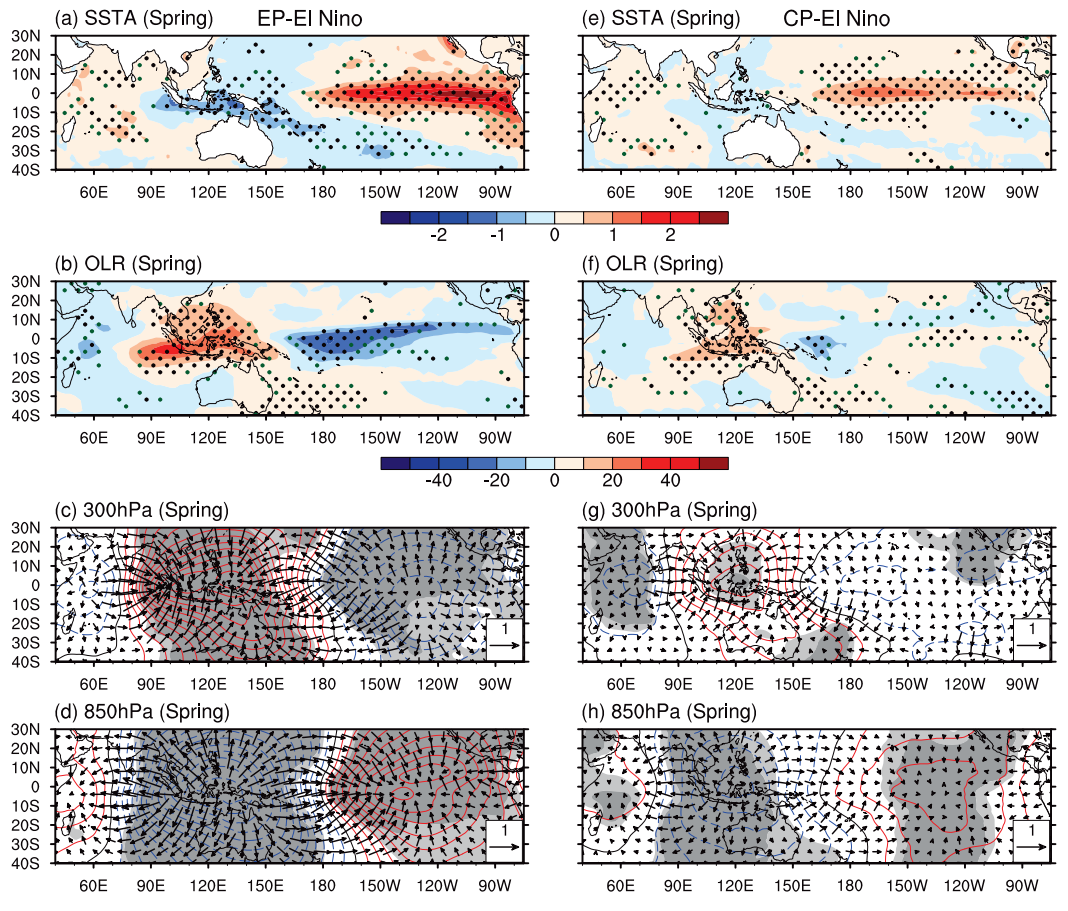


FIG. 3. Composite of (a),(e) NOAA sea surface temperature anomalies (SSTA; unit: $^{\circ}$ C) and (b),(f) NOAA outgoing longwave radiation (OLR) anomalies (unit: W m⁻²), together with the divergent wind (vectors; unit: m s⁻¹) and velocity potential (contours; unit: 10^6 m² s⁻¹; interval: 0.25×10^6 m² s⁻¹) at (c),(g) 300 and (d),(h) 850 hPa, which are calculated by using ERA5, for (left) EP and (right) CP El Niño events. Positive OLR anomaly indicates downward. Red solid, black solid, and blue dashed lines for velocity potential indicate the positive, zero, and negative anomalies, respectively. The dark green stippled areas (and light gray shading) and black stippled areas (and dark gray shading) indicate that the results are statistically significant at the 90% and 95% confidence levels, respectively.

correlated with the DMI, with a significant correlation of 0.60 during the period of 1982–2019, indicating that EP El Niño covaries with the positive phase of IOD (Luo et al. 2010).

In the tropics, the upper-tropospheric circulation is very sensitive to the subtle changes of SST; hence the upper-level divergence associated with the tropical forcing plays a key role in driving tropical–extratropical teleconnections (e.g., Sardeshmukh and Hoskins 1988; Ding et al. 2012). At 300 hPa, in response to the tropical SST anomalies associated with EP El Niño, an anomalous divergence occurs over the central and eastern tropical Pacific (Fig. 3c). Meanwhile, an anomalous convergence occurs over the eastern tropical Indian Ocean and western tropical Pacific. The anomalous convergence are separated by the international date line. At 850 hPa, the distribution of velocity potential anomalies is generally opposite to that at 300 hPa (Fig. 3d). This configuration indicates that the tropical SST anomalies force an anomalous ascent over the central and eastern tropical Pacific

along with an anomalous descent over the Maritime Continent. As a result, large-scale deep convection develops over a broad latitudinal band within 10°N–10°S across the central and eastern equatorial Pacific (Fig. 3b). Consistent with the previous studies, the tropical forcing associated with EP El Niño shifts the ascending branch of the Walker circulation eastward and suppresses the convection over the Maritime Continent and the southeastern tropical Indian Ocean, resulting in strong positive OLR anomalies there (Wang et al. 2003).

In comparison, the CP El Niño is characterized by maximum positive SST anomalies in the central equatorial Pacific (Fig. 2e). The magnitudes of these positive SST anomalies are much smaller than that of EP El Niño. In addition, only a weak positive phase of IOD appears in the tropical Indian Ocean. In the six selected CP El Niño, only two events co-occur with the positive phase of IOD (i.e., the 1994/95 and 2018/19 CP El Niño; Table 1). At the upper level, the anomalous divergence is centered in the central tropical Pacific, with 20°–30° of

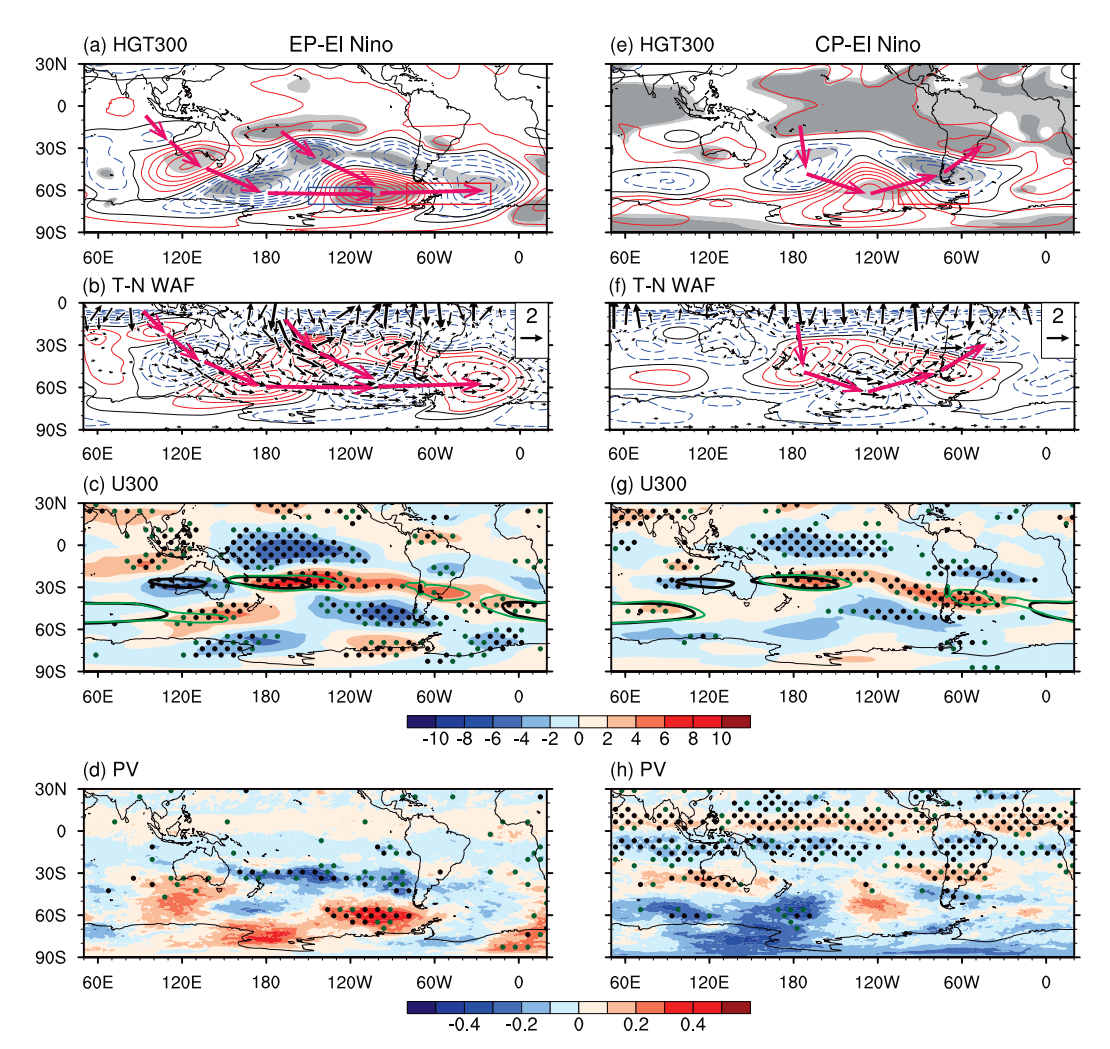


FIG. 4. Composite of (a),(e) 300-hPa geopotential height (HGT300) anomalies (contours; unit: m; interval: 10 m), (c),(g) zonal wind anomalies (shading; unit: m s^{-1}), and (d),(h) potential vorticity (PV) anomalies (shading; unit: $\text{K m}^2 \text{ kg}^{-1} \text{ s}^{-1}$) for (left) EP and (right) CP El Niño events. All the variables are obtained from ERA5. The black and green lines in (c) and (g) indicate the 30 m s^{-1} contours of climatological and composite raw zonal wind, respectively. The dark green stippled areas (and light gray shadings) and black stippled areas (and dark gray shadings) indicate that the results are statistically significant at the 90% and 95% confidence levels, respectively. Red and blue boxes in (a) and (e) are as in Figs. 2a and 2e. (b),(f) The T-N wave activity flux (vectors; unit: $\text{m}^2 \text{ s}^{-2}$), together with 300-hPa streamfunction (contours; interval: 10^6 m s^{-2}). Red solid, black solid, and blue dashed lines indicate the positive, zero, and negative anomalies, respectively.

westward shifting compared with that associated with EP El Niño (Fig. 3g). As a result, the anomalous positive convection induced by the warm SST anomalies is mainly confined to the central Pacific. Similar to EP El Niño, an anomalous sinking also appears over the Maritime Continent (Figs. 3f-h). Both the anomalous positive and negative convection anomalies associated with CP El Niño are much weaker than those associated with EP type. This indicates that, in addition to the tropical Pacific variability, the IOD might be another key factor contributing to the different spatial distributions of SIC anomalies in the West Antarctic between the two types of El Niño.

Previous studies have shown that the warm SST anomalies in the tropical Pacific associated with El Niño, even the descending anomalies in the regions across the southeastern tropical Indian Ocean and Maritime Continent and South Pacific convergence zone (SPCZ), can act as effective Rossby wave sources that excite Rossby wave trains at the upper troposphere in both the Southern and Northern Hemispheres, and therefore transport the effects of tropical variability into higher latitudes (e.g., Karoly and Hoskins 1983; Wang et al. 2003; Clem and Renwick 2015; Clem et al. 2019). The PSA pattern is a part of the Rossby wave train in the Southern Hemisphere. In EP El Niño, the distributions of 300-hPa geopotential height anomalies are characterized by a PSA pattern emanating from the southwestern subtropical Pacific and propagating southeastward into the southeastern Pacific, with a positive (southwestern tropical Pacific)–negative (far east of New Zealand)–positive

(Amundsen–Bellingshausen Seas) center structure (Fig. 4a). This upper-level PSA pattern is a part of the Rossby wave train and is equivalent barotropic in the Southern Hemisphere (Cai et al. 2011).

As for CP El Niño, the 300-hPa geopotential height field bears a resemblance to that in EP El Niño (Fig. 4e). However, the PSA pattern is much weaker in amplitude and has a westward shift compared with EP El Niño, especially for the anomalous positive center in the eastern Ross–Amundsen Seas. In EP El Niño, in addition to the PSA pattern in the South Pacific, a Rossby wave train with a positive–negative–positive–negative center structure, which emanates from the equatorial Indian Ocean and propagates southeastward into the ADP region, can also be found in the southeastern Indian Ocean (Fig. 4a). This IOD-generated Rossby wave train finally merges with the Rossby wave train that forced by EP El Niño in the ADP region. However, no such Rossby wave train appears in the south Indian Ocean in CP El Niño (Fig. 4e).

To further examine the Rossby wave pathway, the horizontal T-N wave activity fluxes associated with the two types of El Niño are calculated based on Eqs. (1) and (2). From Fig. 4b, it is clear that the tropical heat sources associated with EP El Niño and IOD excite two branches of Rossby wave trains that propagate southeastward, resulting in a positive and negative anomaly center at upper level over the eastern Ross-Amundsen-Bellingshausen Seas and the Weddell Sea, respectively. In comparison, only one Rossby wave train emanating from the central tropical Pacific is observed in CP El Niño (Fig. 4f), which results in a positive anomaly center in the eastern Ross-Amundsen Seas, 20° west of that caused by EP El Niño. This indicates that both EP El Niño and IOD can work together to affect the sea ice in the West Antarctic via Rossby wave trains. Although a weak IOD occurs in CP El Niño, the tropical Indian Ocean variability might not be strong enough to induce an equivalent Rossby wave train propagating southeastward.

In a case of El Niño, locations of tropical heat sources play an important role in modulating the location and pathway of the Rossby wave train in the Southern Hemisphere (e.g., Ashok et al. 2007b; Hitchman and Rogal 2010). Positive SST anomalies in the tropical Pacific can enhance tropical convection and the meridional equator-to-polar thermal gradient, and thus strengthen and contract the Hadley cell in the South Pacific (e.g., Yuan 2004). As a result, the subtropical jet in the South Pacific is strengthened and shifted equatorward. In EP El Niño, the center of tropical Pacific anomalous convection is located in 160°-120°W (Figs. 3b-d). Accordingly, the subtropical jet located to the east of Australia along 30°S latitude is strengthened and has an eastward extension compared with the climatological subtropical jet (Fig. 4c). In addition, weak and strong negative potential vorticity (PV) anomalies occur in the north and south of the subtropical jet, respectively (Fig. 4d). Such a gradient of PV anomalies along the subtropical jet together with the eastward extension of the subtropical jet provides favorable conditions for the Rossby wave generation and southeastward propagation, which allows the Rossby wave to pass through 30°S latitude within 160°–120°W (Figs. 4a,b).

In CP El Niño, the anomalous tropical convection is only confined in the western equatorial Pacific, 20°-30° west of that

caused by EP El Niño (Figs. 3f-h). The corresponding subtropical jet is relatively weak with its location shifts westward by 20° in longitude (ends at 100°W) compared with EP El Niño (Fig. 4g). Similar to EP El Niño, weak and strong negative PV anomalies occur in the north and south of the subtropical jet, respectively, with their locations shifting southwestward (Fig. 4h). In particular, the strong negative PV anomalies are centered in the southeast of New Zealand, which locate far southwest of those associated with EP El Niño. Therefore, the Rossby wave pathway generated by CP El Niño has a westward shift compared with EP El Niño, thus resulting in a westward shifted anomalous positive center in the eastern Ross-Amundsen Seas. This also indicates that the different longitudinal locations of the anomalous positive centers associated with two types of El Niño in the West Antarctic can be attributed to the different locations of the tropical heat sources. In addition to the Pacific subtropical jet, a polar front jet centered near 50°S, can also be found in the south Indian Ocean (Figs. 4c,g). In EP El Niño, the polar front jet extends eastward to 150°E, which locates far east compared with CP El Niño (ends in 120°E). This indicates that the eastward extension polar front jet associated with EP El Niño might provide a favorable condition for the Rossby wave generated by IOD to propagate into the South Pacific.

The above analysis suggests that the different distributions of tropical heat sources between the two types of El Niño play important roles in causing the different spatial distributions of SIC anomalies in the West Antarctic. To further verify the links between the tropics and Antarctic sea ice, the maximum covariance analysis (MCA) is employed to capture the dominant coupled modes between SST anomalies in the tropical Indian and Pacific Oceans (15°N-15°S, 40°E-70°W) and 300-hPa geopotential height anomalies in the Southern Hemisphere (0°–90°S) during the period of 1982–2018. Results derived from MCA consist of pairs of spatial modes and corresponding time series, which represent covarying tropical SST and geopotential height structures (e.g., Ding et al. 2011). Similar to previous studies, MCA between these two fields is achieved by performing singular value decomposition on the temporal covariance matrix (e.g., Bretherton et al. 1992; Ding et al. 2011; Okumura et al. 2012). After decomposing, the geopotential height modes can be physically interpreted as the response to the associated tropical SST modes (Ding et al. 2012).

As shown in Fig. 5, the first MCA mode (mode 1) explains 75.6% of the total covariance. The tropical SST mode appears as a zonal tripole pattern with positive SST anomalies over the western Indian Ocean and the central and eastern tropical Pacific and negative SST anomalies over the southeastern tropical Indian Ocean and Maritime Continent and western equatorial Pacific, bearing a resemblance to the distribution of composite SST anomalies associated with EP El Niño (Fig. 5a). Similar to the composite geopotential height pattern, the corresponding geopotential height mode is dominated by a structure of two wave trains in the Southern Hemisphere: one from the southwestern subtropical Pacific and one from the eastern equatorial Indian Ocean (Fig. 5a). Both the wave trains propagate southeastward and culminate to produce a positive and a negative anomaly center over the eastern Ross-

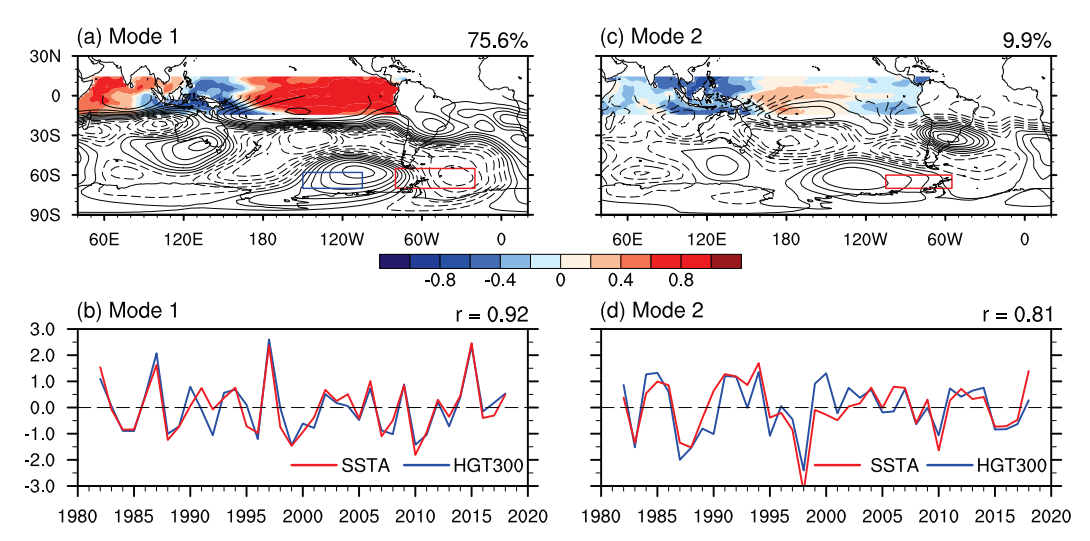


FIG. 5. (a),(c) Patterns and (b),(d) time series associated with the first and second modes (modes 1 and 2) obtained from the maximum covariance analysis (MCA) of detrended SST in the tropical Indian and Pacific Oceans (15°N–15°S, 40°E–70°W; shading) and 300-hPa geopotential height anomalies in the Southern Hemisphere (0°–90°S; contours; interval: 0.1) during austral spring for the period of 1982–2018. In (a) and (b), black solid and dashed lines indicate the positive and negative anomalies, respectively. Red and blue boxes are same as in Figs. 2a and 2e. The values in the top-right corner in (a) and (c) are the explained variances of mode 1 and mode 2, respectively, and in (b) and (d) are the correlation coefficients between the two time series.

Amundsen-Bellingshausen Seas and the Weddell Sea, respectively. This geopotential height mode closely resembles the distribution of composite geopotential height anomalies associated with EP El Niño. In addition, the spatial pattern of correlations between the time series of the tropical SST mode (red line in Fig. 5b) and 300-hP geopotential height anomalies agrees well with both the geopotential height mode obtained from MCA and the distribution of composite geopotential height anomalies (Figs. 4a, 5a, and 6a). This indicates that the anomalous circulation in the Southern Hemisphere can be attributed to the tropical forcing. The high correlation (r = 0.92)between the two time series associated with mode 1 can also verify the links between the tropical SST anomalies and anomalous atmospheric circulation in the Southern Hemisphere (Fig. 5b). It is worth noting that the time series of the tropical SST mode show significant negative and positive correlations with SIC anomalies over the eastern Ross-Amundsen Seas and the Bellingshausen-Weddell Seas, respectively, which are consistent with the composite analysis (Fig. 6c). This further confirms that both EP El Niño and IOD can work together to influence the sea ice through Rossby wave trains.

The second MCA mode (mode 2) explains 9.9% of the total covariance. In contrast with mode 1, the strongest signal in the tropical SST mode is a warming in the central tropical Pacific, with the corresponding geopotential height mode displaying a poleward-arching wave train structure in the South Pacific (Fig. 5c). No obvious wave train can be found in the south Indian Ocean. Similar to the composite analysis, the wave train structure in the South Pacific is much weaker in amplitude and has a westward shift compared with that associated with mode 1. As a result, a relative weak positive anomaly center occurs in the eastern Ross–Amundsen Seas with its location shift

westward by 20° in longitude. The spatial pattern of correlations between the time series of the tropical SST mode (red line in Fig. 5d) and 300-hPa geopotential height anomalies bears a resemblance to both the geopotential height mode and the pattern of composite geopotential height anomalies (Figs. 4e, 5c, and 6d). In addition, significant positive correlations between this time series and SIC anomalies can be observed in the Bellingshausen Sea, which agree well with the composite result (Fig. 6f). However, in addition to these positive correlations, the time series is also significantly negatively correlated with the SIC anomalies in the western Ross Sea and positively correlated with those in the Weddell Sea, where significant and insignificant positive SIC anomalies, respectively, can be seen in the composite analysis. Despite the difference between the MCA and composite analysis, the mode 2 overall can also verify the impacts of CP El Niño on the Antarctic sea ice, especially the westward shift of the Rossby wave train.

Considering the fact that no two El Niño events as well as their impacts are exactly alike due to the diversity and complexity of ENSO (e.g., Timmermann et al. 2018; Okumura 2019). We also examine the uncertainties of the composite analysis which might be caused by individual El Niño events (figure not shown). As for EP El Niño, 1982/83, 1997/98, and 2015/16 El Niños are the three strongest events. Therefore, the amplitudes and domains of positive SST anomalies in the tropical Pacific associated with these three events are much larger than those associated with 1991/92 and 2006/07 El Niño. The 1997/98 and 2006/07 El Niños are accompanied by relatively strong positive phase of IOD compared with the other three events. In the West Antarctic, the intensities of negative SIC anomalies in the eastern Ross–Amundsen Seas (i.e., the

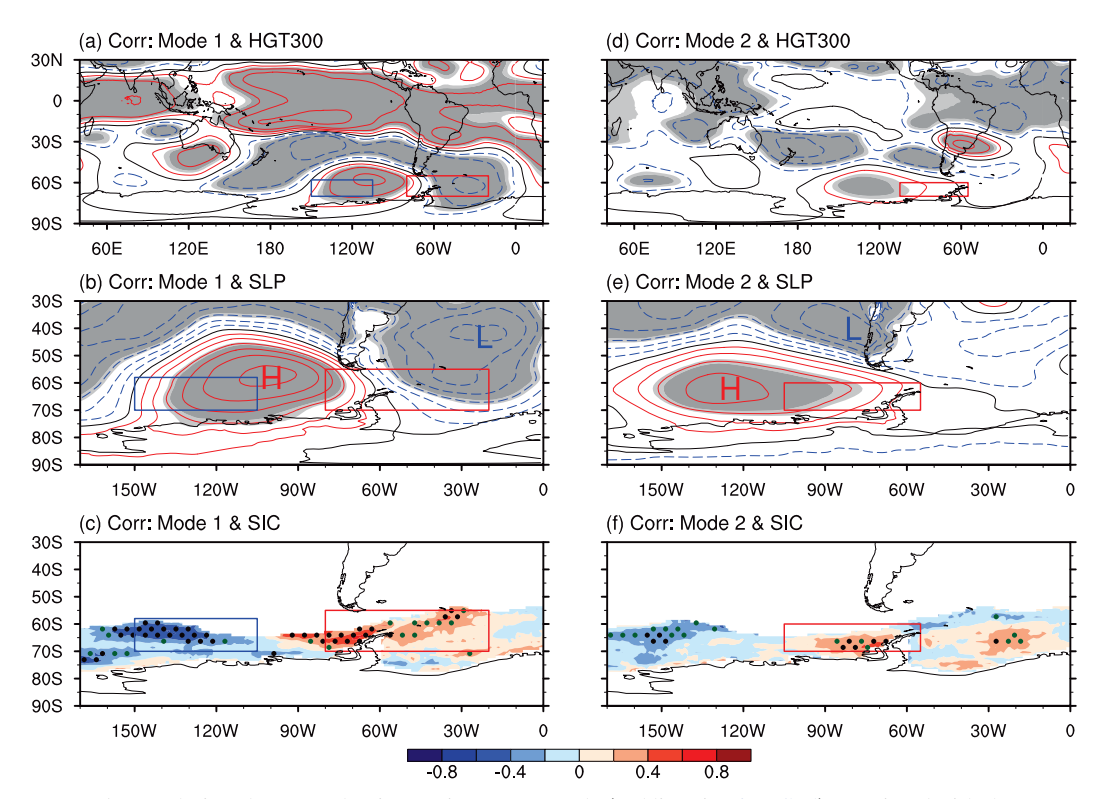


FIG. 6. Correlations between the time series of SST mode (red lines in Figs. 5b,d) associated with the MCA (left) mode 1 and (right) mode 2 and (a),(d) 300-hPa geopotential height anomalies (contour; interval: 0.2), (b),(e) sea level pressure (SLP) anomalies (contour; interval: 0.1), and (c),(f) SIC anomalies. SLP and geopotential height fields are obtained from ERA5, and SIC is obtained from the Hadley Centre. Red solid, black solid, and blue dashed lines indicate the positive, zero, and negative anomalies, respectively. The dark green stippled areas (and light gray shading) and black stippled areas (and dark gray shading) indicate that the results are statistically significant at the 90% and 95% confidence levels, respectively. Red and blue boxes are as in Figs. 2a and 2e.

west pole of the SIC dipole pattern) associated with the 1982/83, 1997/98, and 2006/07 El Niños are stronger than those associated with the other two events. In the Bellingshausen-Weddell Seas (i.e., the east pole of the SIC dipole pattern), the intensities of positive SIC anomalies associated with the 1991/98, 1997/98, and 2015/16 El Niños are stronger than those associated with the other two events, especially for 2015/16 El Niño in which the positive SIC anomalies are strongest. Besides, the impacts of individual EP El Niño events are characterized by large uncertainties outside the West Antarctic. For examples, strong positive SIC anomalies occur in the western Pacific sector during the 1982/83, 2006/07, and 2015/16 El Niños, whereas only weak negative and weak positive SIC anomalies occur during 1991/92 and 1997/98 El Niños, respectively. In addition, strong positive SIC anomalies occur in the Indian Ocean sector during 2006/07 El Niño, whereas no obvious or only weak negative SIC anomalies occur during the other four events. The above analysis indicates that the distributions of the tropical SST anomalies associated with the five selected EP El Niño are similar. Although these EP El Niño events behave with small differences in amplitudes and areas of SST anomalies, they have similar impacts on the sea ice in the West Antarctic.

As for CP El Niño, the positive SST anomalies are centered near the international date line in 1994/95, 2002/03, 2004/05,

and 2009/10 El Niño. In 2002/03 El Niño, the intensities of SST anomalies are the strongest. In comparison, in 2014/15 and 2018/19 El Niño the entire equatorial region is dominated by weak positive SST anomalies. Besides, no obvious IOD events can be found in the Indian Ocean except the 1994/95 and 2018/19 El Niños, which co-occurred with weak positive phase of the IOD. In the West Antarctic, all the selected six CP El Niño events can cause positive SIC anomalies in the Bellingshausen Sea but with different amplitudes. The positive SIC anomalies associated with the 2004/05 El Niño are relatively small compared with the other five events. Different impacts can be observed in other regions. For instance, almost entire Antarctic is dominated by positive SIC anomalies in the 2009/10, 2014/15, and 2018/19 El Niños, while in other events only several parts are characterized by positive anomalies. The above indicates that CP El Niños have similar impacts on the SIC anomalies in the Bellingshausen Sea. Overall, all the five selected EP El Niño or six selected CP El Niños have similar impacts on the SIC anomalies in the West Antarctic in spite of the differences in amplitude of these SIC anomalies. This can also be verified by the significate test of composite analysis passing 90% or 95% confidence levels, and thus further confirms that the composite results are robust.

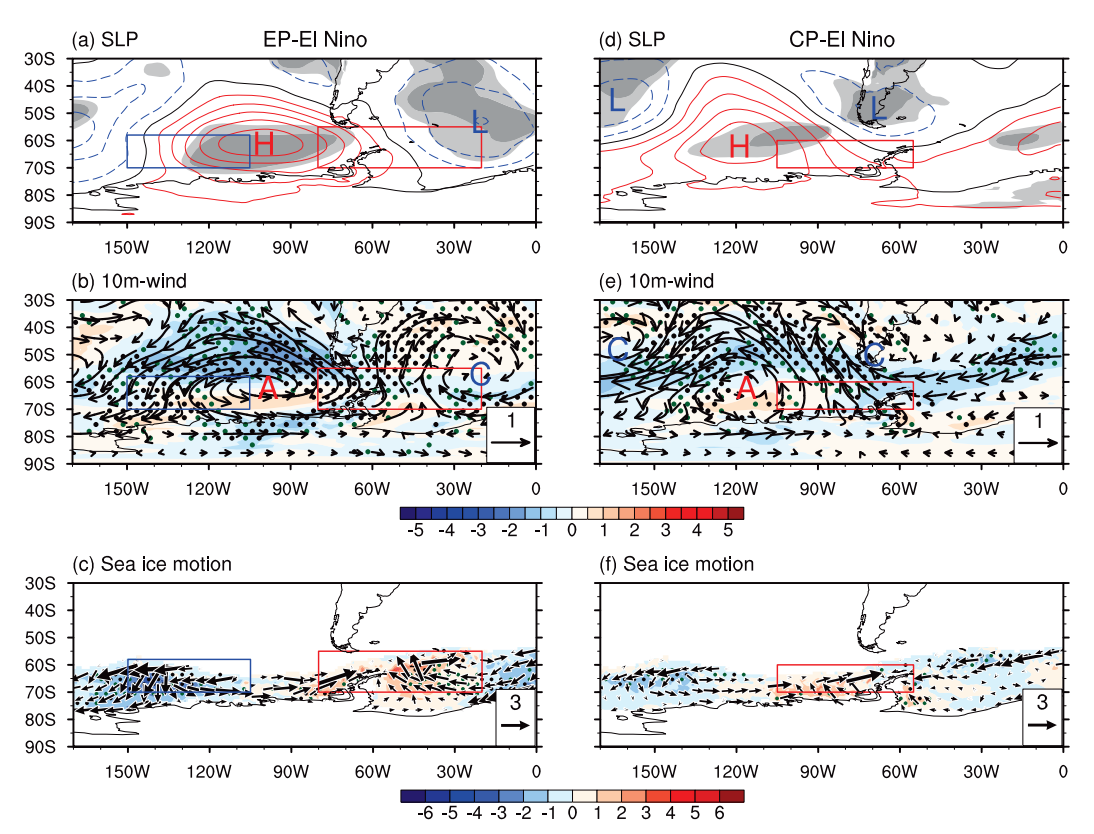


FIG. 7. Composite of (a),(d) SLP anomalies (interval: 1 hPa; unit: hPa), (b),(e) anomalous winds (vectors) together with wind speed anomalies (shading) at 10 m (unit: m s⁻¹), and (c),(f) anomalous sea ice velocity (vectors) together with its meridional component (shading; unit: cm s⁻¹) for (left) EP and (right) CP El Niño events. SLP and wind fields are obtained from ERA5, and sea ice velocity is obtained from ORAS5. Red solid, black solid, and blue dashed lines in (a) and (d) indicate the positive, zero, and negative anomalies, respectively. The dark green stippled areas (and light gray shading) and black stippled areas (and dark gray shading) indicate that the results are statistically significant at the 90% and 95% confidence levels, respectively. Red and blue boxes are as in Figs. 2a and 2e.

4. Possible mechanism

Previous studies have shown that anomalous wind associated with the atmospheric circulation plays important roles in affecting the distribution of sea ice (e.g., Wassermann et al. 2006; Holland and Kwok 2012). First, the wind-driven sea ice drift effect (i.e., atmospheric dynamic effects) modulates the sea ice motion and thus leads to the sea ice growth or melting (e.g., Ding et al. 2011; Holland and Kwok 2012; Wang et al. 2019b). Second, the anomalous wind can affect sea ice via the horizontal heat advection (i.e., the atmospheric thermal effects; Turner et al. 2017). Both cold air in the Antarctic and warmer air or SST in the lower latitudes can be advected into the ADP region by the anomalous wind (Naveira Garabato et al. 2016; Pellichero et al. 2018; Vernet et al. 2019).

In EP El Niño, the tropical heat sources associated with EP El Niño and IOD excited two branches of Rossby wave trains that propagated southeastward, acting as weakening the ASL and resulting in a positive and negative SLP anomaly center (i.e., the anomalous anticyclone and cyclone, respectively) over the eastern Ross-Amundsen-Bellingshausen Seas and Weddell Sea, respectively (Fig. 7a). Strong northerly and

southerly wind anomalies appear to the west and east of the anomalous anticyclone, respectively, where significant negative and positive SIC anomalies can be observed (Figs. 2a and 7b). In comparison, the CP El Niño only causes a relative weak anticyclone anomaly in the eastern Ross-Amundsen Seas, with 20° of westward shifting compared with that caused by EP El Niño (Fig. 7d). The result is consistent with the previous study (Clem et al. 2017), which suggested that SST anomalies centered in the tropical Pacific can force a westward shifted circulation anomaly in the South Pacific compared to the SST anomalies located in the eastern tropical Pacific. Significant southerly wind anomalies appear to the east of the anomalous anticyclone in which positive SIC anomalies occur (Figs. 2e and 7e). These indicate that the anomalous meridional wind associated with the anomalous anticyclone is a key factor to cause different impacts of EP El Niño and CP El Niño on the SIC anomalies in the West Antarctic.

Figure 7 also shows the anomalous sea ice velocity associated with the two types of El Niño. In EP El Niño, strong southerly wind anomalies appear to the east of the anomalous anticyclone, providing a favorable condition for the offshore movement of sea ice in the Bellingshausen–Weddell Seas (Fig. 7c). This

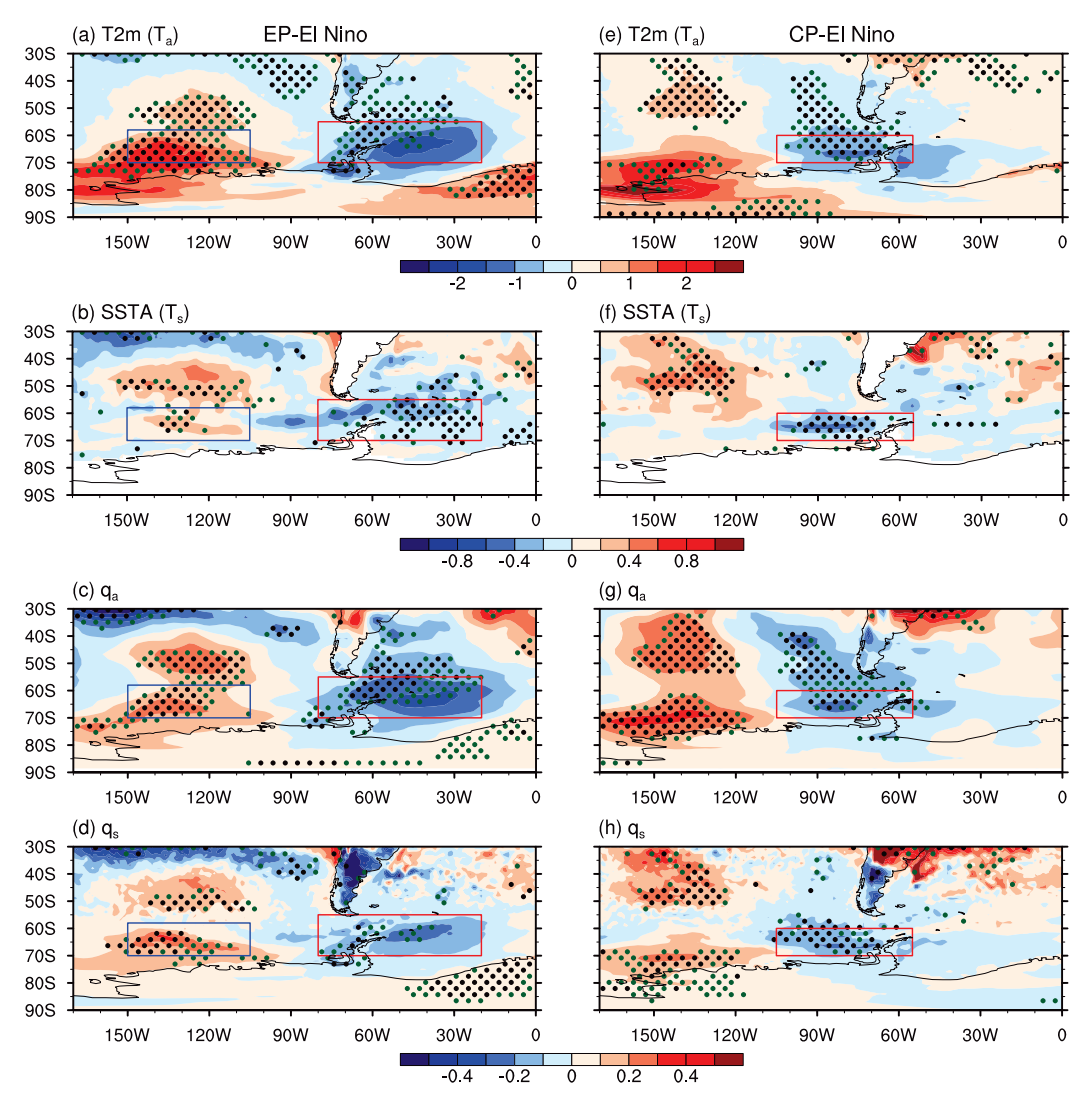


FIG. 8. Composite of (a),(e) temperature anomalies at 2 m (T_a ; unit: °C), (b),(f) SST anomalies (T_s), and specific humidity anomalies (unit: g kg⁻¹) at (c),(g) 2 m (T_s) and (d),(h) the surface (T_s) for (left) EP and (right) CP El Niño events. T2m and T_s are obtained from ERA5, and T_s are obtained from the NCEP-NCAR I. The dark green and black stippled areas indicate that the results are statistically significant at the 90% and 95% confidence levels, respectively. Red and blue boxes are as in Figs. 2a and 2e.

indicates that part of the increased sea ice in the Bellingshausen—Weddell Seas can be attributed to the enhanced northward sea ice drifts driven by the strong southerly wind anomalies. In contrast, significant northerly wind anomalies occur to the west of the anomalous anticyclone. These northerly wind anomalies generate a very strong southward sea ice transport and thus contribute to the sea ice loss in the eastern Ross–Amundsen Seas. As for CP El Niño, anomalous southerly wind to the east of the anomalous anticyclone plays an important role in causing the positive SIC anomalies in the Bellingshausen Sea, which similar to the role of the anomalous southerly wind caused by EP El Niño in the Bellingshausen—Weddell Seas. Therefore, the atmospheric dynamic effects play important roles in causing the different distributions of sea ice in the two types of El Niño via the wind-driven sea ice drift effect.

In addition to the atmospheric dynamic effects, the atmospheric thermal effects could also modulate the sea ice in the West Antarctic through the wind-induced horizontal heat advection. Figure 8 shows the temperature anomalies at 2 m (T2m) and at the surface (SST) together with the specific humidity anomalies at 2 m (q_a) and at the surface (q_s). In EP El Niño, the distributions of both the temperature and specific humidity anomalies are characterized by dipole structures in the ADP region, with a positive anomaly center in the eastern Ross–Amundsen Seas and a negative anomaly center in Bellingshausen–Weddell Seas (Figs. 8a–d), which agree well with the dipole distribution of SIC anomalies.

In the Pacific sector of the Antarctic (i.e., the west pole of the SIC dipole pattern) during EP El Niño, warmer and wetter air together with warmer SST appear in the lower latitudes of the

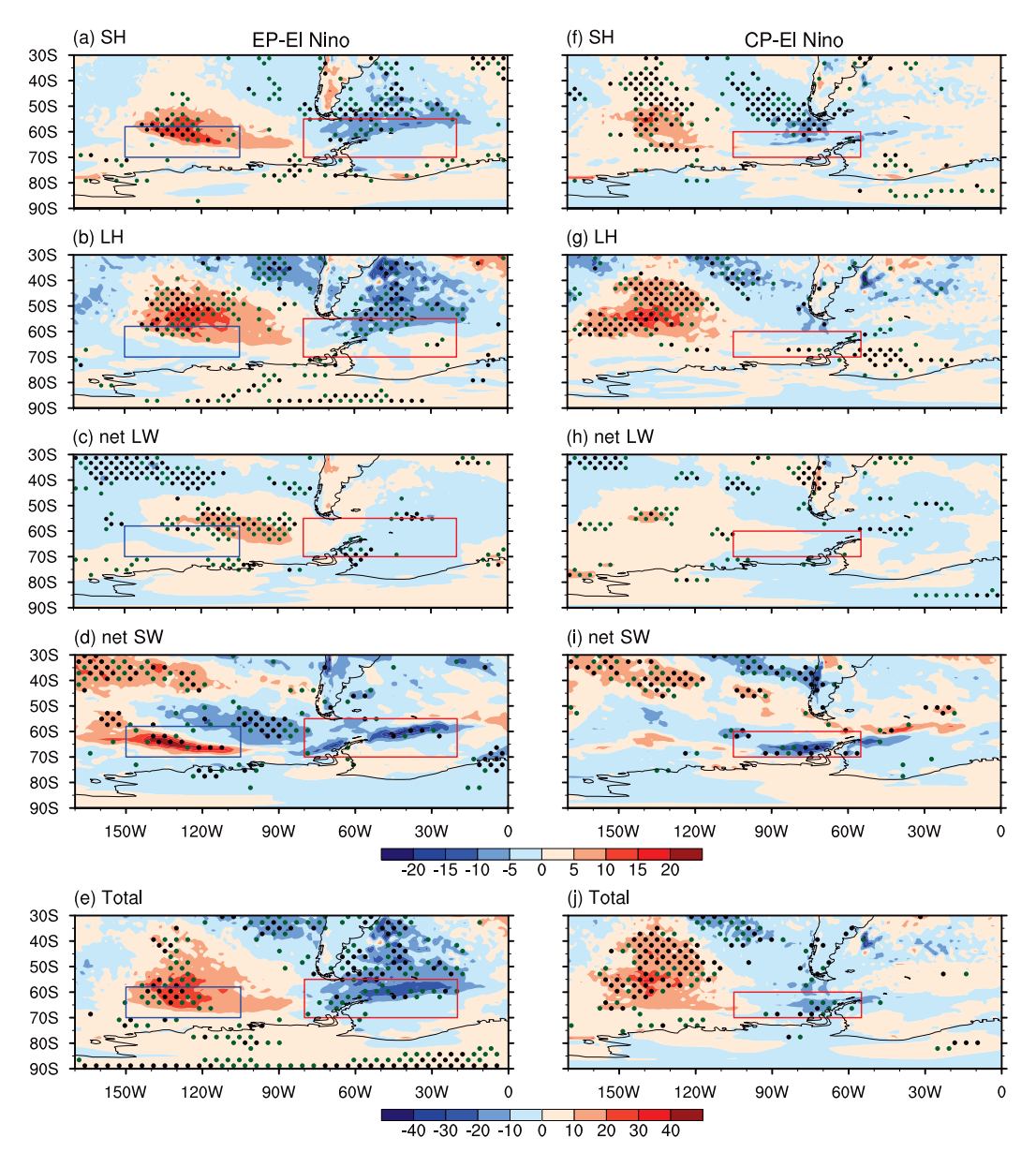


FIG. 9. Composite of surface (a),(f) sensible heat (SH) and (b),(g) latent heat (LH) flux anomalies, and (c),(h) net longwave (LW) and (d),(i) net shortwave (SW) radiation flux anomalies, and (e),(j) total surface heat flux anomalies for (left) EP and (right) CP El Niño events. All the surface heat fluxes are obtained from the ERA5 reanalysis. Total surface heat flux anomalies are equal to the sum of LH, SH, net LW, and net SW anomalies. Positive anomalies indicate downward. Units are W m $^{-2}$. The dark green and black stippled areas indicate that the results are statistically significant at the 90% and 95% confidence levels, respectively. Red and blue boxes are the same as in Figs. 2a and 2e.

South Pacific (Figs. 8a–d). These warmer anomalies play two important roles in shaping the negative SIC anomalies in the eastern Ross–Amundsen Seas. First, both the warmer air and SST in lower latitudes can be advected into the eastern Ross–Amundsen Seas by the strong northerly wind anomalies to the west of the anomalous anticyclone, acting as melting sea ice there. Second, the amplitudes of T2m and q_a anomalies (Figs. 8a,c) in the regions with negative SIC anomalies (i.e., the area in the blue box) are greater than that of SST and q_s

anomalies (Figs. 8b,c). This indicates that the warmer and wetter air can also result in an increase in surface SH and LH fluxes, respectively, in the eastern Ross–Amundsen Seas (Figs. 9a,b). The increased surface SH and LH fluxes further cause surface warming and thus result in negative SIC anomalies. From Fig. 10, we can find that both the positive surface SH and LH flux anomalies contribute to the sea ice loss in the eastern Ross–Amundsen Seas, especially the surface SH flux.

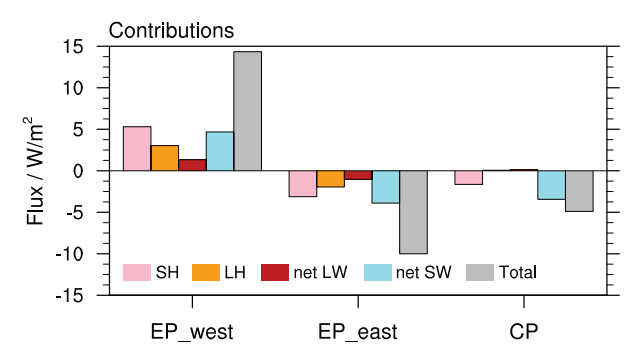


FIG. 10. Contributions of SH (pink bars), LH (orange bars), net LW (brown bars), and net SW (light blue bars) together with the total surface heat flux (gray bars) to the distributions of SIC anomalies associated with EP El Niño and CP El Niño. The contributions are estimated by the averaged anomalies over the blue (EP_west) and red (EP_east) boxes in Figs. 9a–e for EP El Niño, and the red box (CP) in Figs. 9f–j for CP El Niño. Units are W m $^{-2}$.

In addition, the increased net SW radiation flux is another important contributor in shaping the negative SIC anomalies, which play a comparable role with that of the increased surface SH flux (Figs. 9d and 10). In the eastern Ross–Amundsen Seas, the induced warm SST anomalies also play an important role in reducing the cloud covers in the lower and middle levels of the troposphere (Wu and Kinter 2010). As shown in Fig. 11a, significant negative cloud coves anomalies can be observed in the region covered by negative SIC anomalies. As a result, this reduced cloudiness favors an increase in the net SW radiation flux, and thus in turn strengthens the SST warming. This indicates that the positive feedback between SST, net SW radiation flux, and clouds also contributes to the sea ice melting in the eastern Ross-Amundsen Seas through the enhanced SST warming. In comparison, the contribution of net LW radiation flux is small and negligible (Figs. 9c and 10).

As for the Atlantic sector of the Antarctic (i.e., the east pole of the SIC dipole pattern), the significant southerly wind anomalies to the east of the anomalies anticyclone play opposite roles compared with the northerly wind anomalies to the west. Cold and dry advection to the east of the anomalous anticyclone

generates cold temperatures in the Bellingshausen-Weddell Seas through the reduced surface SH and LH heat fluxes, which leads to a positive SIC anomaly (Figs. 8a-d, 9a-e, and 10). In addition, the negative net SW radiation flux anomalies contribute a large fraction to the total surface heat flux anomaly, which acts to increase the SIC anomalies in the Bellingshausen-Weddell Seas (Figs. 9d and 10). This is because that the negative SST anomalies can lead to an increase in cloud cover, which reduces the net SW and in turn strengthens the SST cooling. As a consequence, sea ice is increased. However, the role of net LW radiation flux is less important compared with the other radiation flux heat fluxes (Figs. 9c and 10). Therefore, the warm and wet (cold and dry) advection to the west (east) of the anomalous anticyclone associated with EP El Niño plays important roles in shaping the SIC dipole pattern in the West Antarctic.

In CP El Niño, the anomalous convection in the tropical Pacific has a westward shift compared with that caused by EP El Niño. Consequently, the Rossby wave train forced by the anomalous heating also shifts to the west, resulting in a westward-shifted anomalous anticyclone in the eastern Ross-Amundsen Seas (Fig. 7d), 20° west of that caused by EP El Niño. As a result, unlike the dipole pattern of SIC anomalies generated by EP El Niño, only positive SIC anomalies occur in the Bellingshausen Sea (Fig. 2e). Anomalous southerly wind to the east of the anomalous anticyclone centered in the Amundsen Sea plays an important role in causing these positive SIC anomalies (Fig. 7e), similar to the role of the anomalous southerly wind caused by EP El Niño in the Bellingshausen-Weddell Seas. Cold advection to the east of the anomalous anticyclone yields negative temperature anomalies through the reduced surface SH flux (Figs. 8e,f and 9f), which contributes to the sea ice growth in the Bellingshausen Sea (Figs. 9j and 10). In addition, significant positive cloud cover anomalies appear in the Bellingshausen Sea due to the significant negative SST anomalies (Fig. 11b). These increased cloud covers in turn cool the ocean surface through the reduced net SW radiation flux, which ultimately contribute to the positive SIC anomalies in the Bellingshausen Sea (Figs. 9i and 10). In comparison, the surface LH flux and net LW radiation flux contributions are minor (Figs. 9g,h and 10). Therefore, the reduced surface SH flux and net SW radiation flux are the two key factors for generating the positive SIC anomalies in the Bellingshausen Sea.

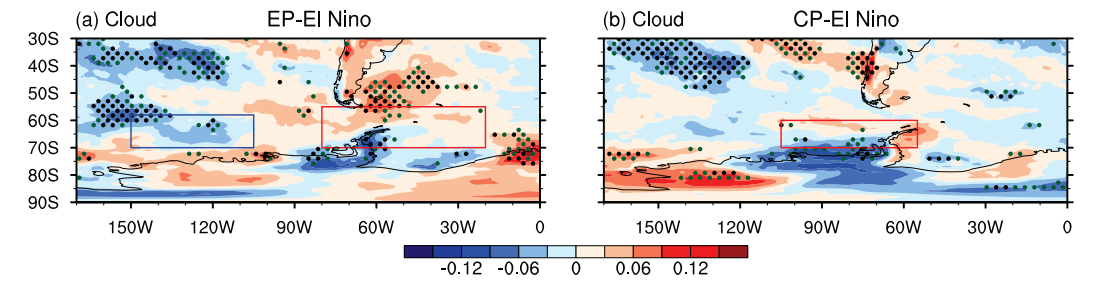


FIG. 11. Composite of the sum of ERA5 medium and low cloud-cover anomalies for (a) EP and (b) CP El Niño events. The dark green and black stippled areas indicate that the results are statistically significant at the 90% and 95% confidence levels, respectively. Red and blue boxes are as in Figs. 2a and 2e.

TABLE 2. Six experiments conducted with the dry version of the Princeton AGCM.

Expt Initiated heating Ex_EP Tropical Indian Ocean and Pacific (20°N-80°W) of EP El Niño Ex_EP _{Ind} Tropical Indian Ocean alone (20°N-20°S	
80°W) of EP El Niño	
Ex_EP _{Ind} Tropical Indian Ocean alone (20°N–20°S	-20°S, 40°E-
of EP El Niño	, 40°–120°E)
Ex_EP _{Pac} Tropical Pacific alone (20°N–20°S, 120°F EP El Niño	E–80°W) of
Ex_CP Tropical Indian Ocean and Pacific (20°N 40°E–80°W) of CP El Niño	V–20°S,
Ex_CP _{Ind} Tropical Indian Ocean alone (20°N–20°S of CP El Niño	, 40°–120°E)
$\begin{array}{ccc} Ex_CP_{Pac} & Tropical \ Pacific \ alone \ (20^{\circ}N-20^{\circ}S, 120^{\circ}K) \\ & CP \ El \ Ni\~no \end{array}$	∃–80°W) of

5. Responses of atmospheric circulation to the tropical heating

The above shows that both EP El Niño and CP El Niño can affect the sea ice in the West Antarctic through Rossby wave trains (Fig. 4). To verify the responses of atmospheric circulation in the Southern Hemisphere to the anomalous tropical heating associated with the two types of El Niño, a dry version of the Princeton AGCM was used (Wang et al. 2003; Jiang and Li 2005). We conducted six experiments with the AGCM (Table 2). In the first and second experiments, the AGCM was

initiated with the anomalous heating associated with EP El Niño and CP El Niño, respectively, in both the tropical Indian Ocean and Pacific (20°N–20°S, 40°E–80°W); these experiments are called Ex_EP and Ex_CP, respectively. Anomalous diabatic heating prescribed in the AGCM is based on the OLR pattern during austral spring (Figs. 3b,f). The OLR anomalies were scaled by the value of OLR anomaly with the maximum amplitude within 20°N-20°S, 40°E-80°W during the two types of El Niño (i.e., the maximum amplitude of diabatic heating is 1), as shown in Figs. 12a and 13a. No heating source (diabatic heating = 0) was prescribed in other regions. To estimate the individual role of the tropical Indian Ocean and the tropical Pacific, the third and fourth experiments were initiated with the anomalous heating associated with EP El Niño in the tropical Indian Ocean alone (20°N-20°S, 40°-120°E; Ex_ EP_{Ind}), and the tropical Pacific alone (20°N–20°S, 120°E–80°W; Ex_EP_{Pac}), respectively (Figs. 12b,c and Table 2). The fifth and sixth experiments are similar to the third and fourth experiments, but initiated with the anomalous heating associated with CP El Niño, and are called Ex_CP_{Ind} and Ex_CP_{Pac} , respectively (Figs. 13b,c, and Table 2).

When initiated with the anomalous heating in both the tropical Indian Ocean and Pacific, the atmospheric circulation responses in the Ex_EP and Ex_CP experiments bear resemblances to the results obtained from the composite analysis, especially in the Ex_EP experiment (Figs. 14a,d). This indicates that the tropical heating is the primary factor forcing the anomalous atmospheric circulations. In the Ex_EP

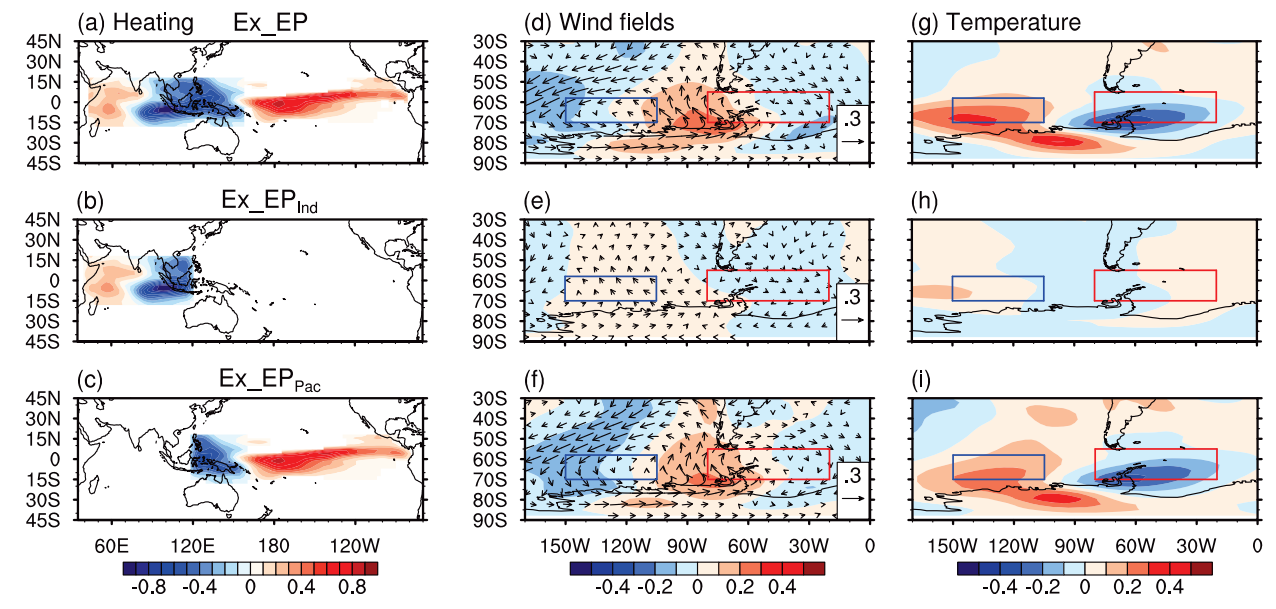


FIG. 12. Responses of (d)–(f) 850-hPa wind field (unit: m s $^{-1}$) and (g)–(i) 850-hPa temperature (unit: °C) to the (a)–(c) anomalous diabatic heating associated with EP El Niño in (top) both the tropical Indian Ocean and Pacific (20°N–20°S, 40°E–80°W; Ex_EP), (middle) the tropical Indian Ocean alone (20°N–20°S, 40°–120°E; Ex_EP_{Ind}), and (bottom) the tropical Pacific alone (20°N–20°S, 120°E–80°W; Ex_EP_{Pac}). The shading in (a)–(c) indicates the initiated anomalous diabatic heating associated with EP El Niño, and in (d)–(f) denotes 850-hPa meridional wind anomalies. Anomalous diabatic heating is calculated based on the OLR pattern during austral spring (Figs. 3b,f). The OLR anomalies are scaled by the value of OLR anomaly with maximum amplitude within 20°N–20°S, 40°E–80°W during the two types of El Niño, i.e., the maximum amplitude of diabatic heating is 1. No heating source (diabatic heating = 0) is prescribed in other regions. These three experiments are conducted with the dry version of the Princeton AGCM. Red and blue boxes are as in Fig. 2a.

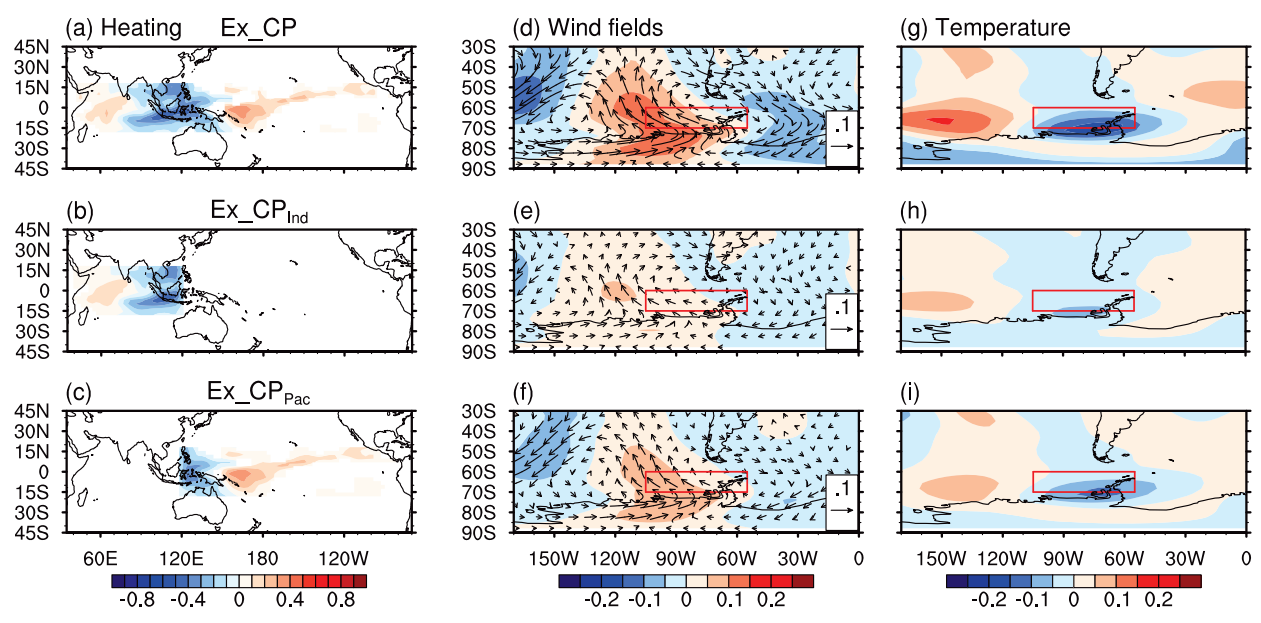


FIG. 13. As in Fig. 12, but for CP El Niño. The three experiments are initiated with the anomalous heating associated with CP El Niño in (top) both the tropical Indian Ocean and Pacific (Ex_CP), (middle) the tropical Indian Ocean alone (Ex_CP_{Ind}), and (bottom) the tropical Pacific alone (Ex_CP_{Pac}). Red boxes are as in Fig. 2e.

experiment, the diabatic heating associated with positive phase of IOD and EP El Niño excites two branches of Rossby wave trains at 300 hPa that propagate southeastward, resulting in an anomalous anticyclone at lower level in the eastern Ross–Amundsen–Bellingshausen Seas (Figs. 12d and 14a). As a result, strong northerly and southerly wind anomalies occur to the west and east of the anomalous anticyclone, respectively (Fig. 12d). Therefore, warm and cold advection to the west and east of the anomalous anticyclone generate positive and negative temperature anomalies in the eastern Ross–Amundsen Seas and Bellingshausen–Weddell Seas, resulting in a sea ice loss and growth, respectively (Figs. 12d,g). This indicates the both the IOD and EP El Niño can work together to cause the SIC dipole pattern in the West Antarctic.

In the Ex_EP_{Ind} experiment initiated with the anomalous heating in the tropical Indian Ocean alone, a wave train-like structure in the 300-hPa geopotential height responses, which emanates from the tropical Indian Ocean and dissipates in the eastern Ross-Amundsen Seas, can be observed (Fig. 14b). Although no evident responses of the wind field and temperature were observed in the ADP region (Figs. 12e,h), this IOD-induced Rossby wave train can generate less positive geopotential height anomalies in the eastern Ross-Amundsen Seas (Fig. 14b), which might contribute to the occurrence of the anomalous anticyclone (Fig. 4a). When initiated with the tropical Pacific heating (i.e., the Ex_EP_{Pac} experiment), an evident Rossby wave train that extends from the central tropical Pacific to the ADP region can be observed (Fig. 14c). This indicates that EP El Niño plays a more important role in generating the dipole structure in SIC anomalies compared with the positive phase of the IOD. Besides, a clear Rossby wave train emanating from the eastern tropical Indian Ocean and propagating southward was captured, indicating that the EP El Niño can first affect the tropical Indian Ocean and then influence the Antarctic sea ice. In other words, the effects of the IOD on the SH are strengthened by EP El Niño, in agreement with previous studies showing that the Rossby wave train can reach to the Bellingshausen Sea, even to the South Atlantic, if the ENSO and IOD events coexist (Cai et al. 2011; Chan et al. 2008). This is because that the tropical Pacific and the tropical Indian Ocean can be connected via the Walker circulation (e.g., Li et al. 2003; Cai et al. 2019). The positive SST anomalies in the tropical Pacific shift the Walker circulation eastward and suppress convection over the southeastern tropical Indian Ocean and the Maritime Continent. As a result, the positive OLR anomalies in the Maritime Continent and the southeastern tropical Indian Ocean are strengthened, which further strengthen the Rossby source associated with IOD. The above shows that both the IOD and EP El Niño can help to generate the anomalous anticyclone in the eastern Ross-Amundsen Seas by exciting Rossby wave trains, but that EP El Niño plays the dominant role.

As for CP El Niño, no evident difference in responses can be found between the Ex_CP and Ex_CP_{Pac} experiments, although they are initiated with different anomalous heating (Figs. 14d,f). Both the Ex_CP and Ex_CP_{Pac} experiments reproduced the strong southerly wind anomalies and negative temperature anomalies in the Bellingshausen Sea (Figs. 13d,f,g,i), which result in positive SIC anomalies there. However, in the Ex_CP_{Ind} experiment, only a very weak Rossby wave train is forced by the anomalous heating in the tropical Indian Ocean alone (Fig. 14e). This Rossby wave train was much weaker than that generated by the IOD associated with EP El Niño (Figs. 14b). In addition, no response was found in the Bellingshausen Sea (Figs. 13e,h). This further verifies that the weak positive IOD associated with CP El

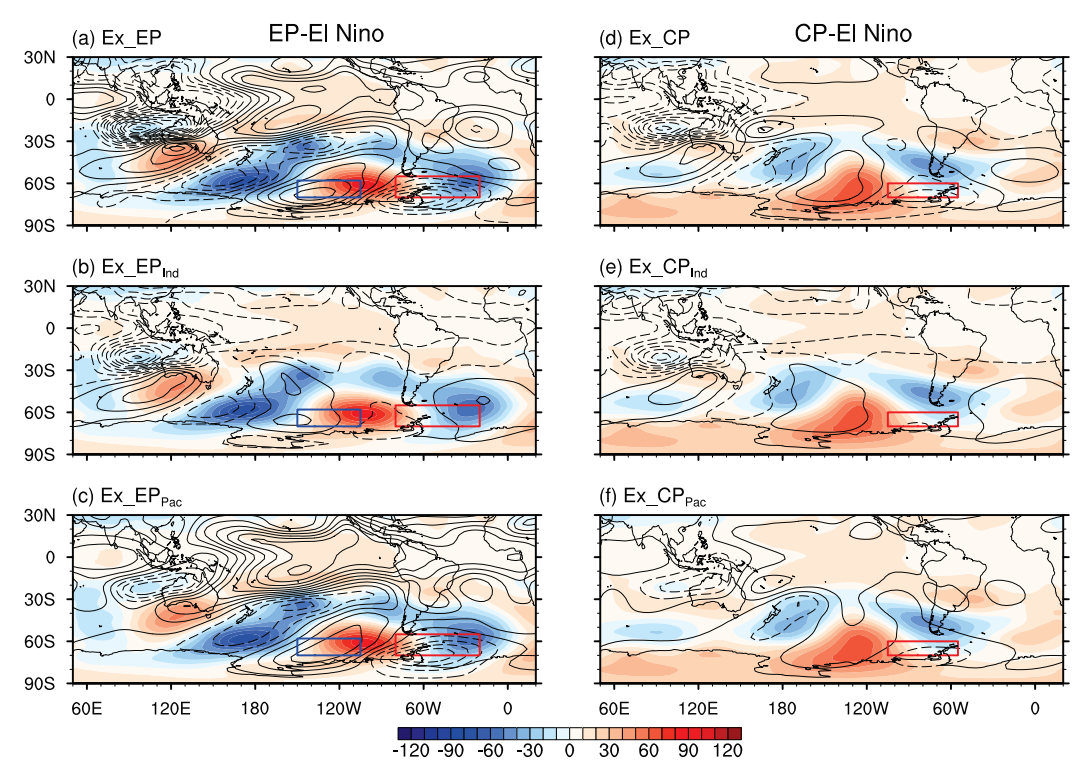


FIG. 14. Responses of 300-hPa geopotential height (contours; unit: m; interval: 10 m) to the anomalous heating associated with EP El Niño in (a) both the tropical Indian Ocean and Pacific, (b) the tropical Indian Ocean alone, and (c) the tropical Pacific alone. (d)–(f) As in (a)–(c), but for the responses associated with CP El Niño. To aid comparison, the composite 300-hPa geopotential height anomalies associated with EP El Niño (Fig. 4a) and CP El Niño (Fig. 4e) are shown again in (a)–(c) and (d)–(f), respectively, with shading (interval: 10 m) rather than contours. Red and blue boxes are as in Figs. 2a and 2e.

Niño has no significant impact on generating positive SIC anomalies in the Bellingshausen Sea.

6. Conclusions

In this study, we found that the CP El Niño and EP El Niño have distinctive impacts on the spatial distributions of SIC anomalies in the Antarctic during austral spring. The EP El Niño caused a dipole distribution of SIC anomalies in the West Antarctic, with negative SIC anomalies in the eastern Ross–Amundsen Seas and positive SIC anomalies in the Bellingshausen–Weddell Seas, which is referred to as the Antarctic dipole (ADP) (Yuan and Martinson 2001). In comparison, the CP El Niño only generated a positive SIC anomaly center in the Bellingshausen Sea. The physical mechanism responsible for such different impacts between the two types of El Niño was investigated through observational data analysis and idealized modeling experiments.

For EP El Niño, all the five selected events co-occurred with a strong positive phase of the IOD. The diabatic heating associated with the positive phase of the IOD and EP El Niño excited two branches of Rossby wave trains that emanated from the tropical Indian Ocean and central tropical Pacific, respectively, and both propagated southeastward. These two Rossby wave trains combined in the South Pacific, resulting in an anomalous anticyclone and an anomalous cyclone over the

eastern Ross-Amundsen-Bellingshausen Seas and the Weddell Sea, respectively (Fig. 7a).

As a result, anomalous northerly and southerly wind to the west and east of the anomalous provide favorable conditions for the poleward and offshore movements of sea ice, respectively, which act as decreasing and increasing the sea ice in the eastern Ross-Amundsen Seas and the Bellingshausen-Weddell Seas. In addition to the wind-driven sea ice drift effect, the atmospheric thermal effects also play important roles. In the west pole of the SIC dipole pattern, warmer and wetter air together with warmer SST in the lower latitudes of the South Pacific are advected into the eastern Ross-Amundsen Seas by the strong northerly wind anomalies to the west of the anomalous anticyclone, causing increases in surface SH and LH fluxes, which acted as melting the sea ice due to the induced surface warming. In addition, the enhanced SST warming also caused a reduction in cloud covers, which in turn strengthened the SST warming via increasing the net SW radiation flux and thus contributed to sea ice melting. In contrast, the significant southerly wind anomalies to the east of the anticyclone played an opposite role. Cold and dry advection to the east of the anomalous anticyclone generated surface cooling in the Bellingshausen-Weddell Seas through the reduced surface SH and LH fluxes and net SW radiation flux, which resulted in positive SIC anomalies. Therefore, the strong northerly

and southerly wind anomalies to the west and east of the anomalous anticyclone caused by EP El Niño play important roles in shaping the dipole pattern in SIC anomalies in the West Antarctic.

In CP El Niño, the anomalous heating to the west of the international date line in the tropical Pacific excited a Rossby wave train that propagated southeastward. Unlike EP El Niño, no Rossby wave train was generated by the weak positive phase of IOD. Therefore, the weak IOD co-occurred with CP El Niño had no impact on the SIC in the West Antarctic. Similar to EP El Niño, the Rossby wave train generated by the anomalous heating in tropical Pacific also caused an anomalous anticyclone in the eastern Ross-Amundsen Seas, 20° west of that caused by EP El Niño (Fig. 7d). Anomalous southerly wind to the east of the anomalous anticyclone played an important role in causing the positive SIC anomalies in the Bellingshausen Sea. Part of the increased sea ice can be attributed to the wind-driven sea ice drift effect, as southerly anomalies in the region would provide a favorable condition for the offshore movement of sea ice in the Bellingshausen Sea. In addition, the reduced surface SH flux, especially the reduced net SW radiation flux, also contributed to the positive SIC anomalies through the induced surface cooling.

The different longitudinal locations of the anomalous anticyclone associated with two types of El Niño in the West Antarctic can be attributed to the different locations of tropical heating sources. In EP El Niño, the anomalous convection occurred in the western Pacific, leading to a strengthened and eastward-extended subtropical jet along 30°S latitude. Weak and strong negative PV anomalies occurred in the north and south of the subtropical jet, respectively. Such gradient of PV anomalies together with the eastward-extended subtropical jet provide favorable conditions for the Rossby wave to pass through the 30°S latitude within 160°–120°W. In comparison, the anomalous tropical convection associated with CP El Niño has a westward shift, 20°-30° west of that associated with EP El Niño. The corresponding subtropical jet is relatively weak with its location shifts westward by 20° in longitude compared with EP El Niño. Therefore, the Rossby wave pathway generated by CP El Niño has a westward shift, resulting in a westward shifted anomalous anticyclone in the eastern Ross-Amundsen Seas.

To further prove the robustness of the composite results, the MCA was employed to capture the dominant coupled modes between the tropical SST anomalies and 300-hPa geopotential height anomalies in the Southern Hemisphere. The first and second MCA modes can well capture the coupled tropical SST anomalies and geopotential height anomalies in the Southern Hemisphere associated with EP El Niño and CP El Niño, respectively. In addition, we also calculated correlations between the time series of the tropical SST modes obtained from MCA and SIC anomalies, geopotential height anomalies, SLP anomalies, temperature anomalies, specific humidity anomalies, surface heat fluxes, and clouds (parts of them are shown in Fig. 6). The special distributions of these correlations agree well with the composite analysis and thus confirm that the composite analysis is robust, although different characteristics exist between individual El Niño events.

In addition, a dry version of the Princeton AGCM was used to verify the links between the two types of El Niño and the SIC in the West Antarctic. The responses of atmospheric circulation in the Southern Hemisphere to the anomalous heating associated with the two types of El Niño bore resemblances to the observed results. When the observed anomalous heating associated with EP El Niño and IOD was specified, two branches of Rossby wave trains emanating from the tropical Indian Ocean and Pacific, respectively, and propagating southeastward were observed. This indicates that IOD and EP El Niño can work together to cause an anomalous anticyclone in the eastern Ross-Amundsen-Bellingshausen Seas through Rossby wave trains. Furthermore, we also estimated the individual roles of the tropical Indian Ocean and Pacific. The EP El Niño played the dominant role in shaping the dipole pattern in SIC anomalies in the West Antarctic. Although no obvious responses of the wind fields and temperatures to the anomalous heating in the tropical Indian Ocean alone can be found, the IOD-induced Rossby wave train can still generate less positive geopotential height anomalies in the eastern Ross-Amundsen Seas, which contributed to the occurrence of the anomalous anticyclone. Besides, the results also showed that the EP El Niño can first affect the tropical Indian Ocean, and then influence the Antarctic sea ice. In other words, the effects of IOD on the SH was strengthened by EP El Niño. In CP El Niño condition, the anomalous heating in tropics only forced a relative weak Rossby wave train emanating from the tropical Pacific, compared with EP El Niño. No responses of wind fields or temperatures in the West Antarctic to the anomalous heating associated with the weak positive phase of IOD can be observed. This further verifies that the positive SIC anomalies in the Bellingshausen Sea were caused by CP El Niño through the Rossby wave train, rather than the weak IOD. Note that the numerical experiments conducted in this study did not perfectly reproduce the composite analysis. For example, the simulated wave train patterns shift westward compared with the composite analysis, especially for the simulated Rossby wave trains in Ex_EP_{Ind} and Ex_CP_{Ind}. Why the simulations have westward shifts in the Southern Hemisphere is not resolved and remains for further research. However, to a large extent, these experiments do support the conclusion that the tropical heating sources associated with EP El Niño and IOD can excite two branches of Rossby wave trains and those associated with CP El Niño excite only one Rossby wave train. In addition, the longitudinal shifting of the Rossby wave trains and anomalous anticyclone can be well captured by

In the study, there are three main reasons that why we focus on the impacts of CP El Niño and EP El Niño on the Antarctic sea ice in austral spring, rather than in other seasons. First of all, IOD tends to peak in austral spring and exhibits different features in CP El Niño and EP El Niño. However, the potential impact of IOD on the sea ice during EP El Niño and CP El Niño is unclear. In this study, we found that the positive phase of IOD also played an important role in contributing to the occurrence of the dipole distribution of sea ice anomalies during EP El Niño, whereas no impact was observed during CP El Niño. This is the novelty of our study. Second, the SIC anomalies in the West Antarctic are characterized by higher

variability in austral spring than in other seasons. Third, the impacts of El Niño on the atmospheric circulation in the Southern Hemisphere and specifically on the Antarctic sea ice are the strongest in austral spring (e.g., Jin and Kirtman 2009; Song et al. 2011; Yuan et al. 2018). Besides, the impacts of the two types of El Niño in other three seasons have been well documented in several previous studies (e.g., Ding et al. 2011; Song et al. 2011; Wilson et al. 2014; Ciasto et al. 2015) and therefore would not be extended in the present study.

Acknowledgments. This work is jointly supported by the Strategic Project of Chinese Academy of Science (Grant XDA19070402), NSFC Grants 42088101 and 41630423, and NSF AGS-2006553. This is SOEST contribution number 11415 and IPRC contribution number 1542.

REFERENCES

- Annamalai, H., S. P. Xie, J. P. McCreary, and R. Murtugudde, 2005: Impact of Indian Ocean sea surface temperature on developing El Niño. *J. Climate*, 18, 302–319, https://doi.org/ 10.1175/JCLI-3268.1.
- Ashok, K., Z. Guan, N. H. Saji, and T. Yamagata, 2004: Individual and combined influences of ENSO and the Indian Ocean dipole on the Indian summer monsoon. *J. Climate*, 17, 3141–3155, https://doi.org/10.1175/1520-0442(2004)017<3141: IACIOE>2.0.CO;2.
- ——, H. Nakamura, and T. Yamagata, 2007a: Impacts of ENSO and Indian Ocean dipole events on the Southern Hemisphere storm-track activity during austral winter. *J. Climate*, 20, 3147–3163, https://doi.org/10.1175/JCLI4155.1.
- —, S. K. Behera, S. A. Rao, H. Y. Weng, and T. Yamagata, 2007b: El Niño Modoki and its possible teleconnection. *J. Geophys. Res.*, **112**, C11007, https://doi.org/10.1029/2006JC003798.
- Bintanja, R., G. J. van Oldenborgh, S. S. Drijfhout, B. Wouters, and C. A. Katsman, 2013: Important role for ocean warming and increased ice-shelf melt in Antarctic sea-ice expansion. *Nat. Geosci.*, 6, 376–379, https://doi.org/10.1038/ngeo1767.
- Bretherton, C. S., C. Smith, and J. M. Wallace, 1992: An intercomparison of methods for finding coupled patterns in climate data. *J. Climate*, **5**, 541–560, https://doi.org/10.1175/ 1520-0442(1992)005<0541:AIOMFF>2.0.CO:2.
- C3S, 2019: C3S ERA5-Land reanalysis. Copernicus Climate Change Service, accessed 2020, https://cds.climate.copernicus.eu/cdsapp#!/dataset/reanalysis-era5-single-levels-monthly-means?tab=overview.
- Cai, W. J., P. Rensch, T. Cowan, and H. H. Hendon, 2011: Teleconnection pathways of ENSO and the IOD and the mechanisms for impacts on Australian rainfall. *J. Climate*, 24, 3910–3923, https://doi.org/10.1175/2011JCLI4129.1.
- —, and Coauthors, 2019: Pantropical climate interactions. *Science*, 363, eaav4236, https://doi.org/10.1126/science.aav4236.
- Carleton, A. M., 1989: Antarctic sea-ice relationships with indices of the atmospheric circulation of the Southern Hemisphere. Climate Dyn., 3, 207–220, https://doi.org/10.1007/ BF01058236.
- Chan, S. C., S. K. Behera, and T. Yamagata, 2008: Indian Ocean Dipole influence on South American rainfall. *Geophys. Res. Lett.*, 35, L14S12, https://doi.org/10.1029/2008GL034204.
- Chen, M., T. Li, and X. Wang, 2019: Asymmetry of atmospheric responses to two-type El Niño and La Niña over Northwest Pacific. *J. Meteor. Res.*, **33**, 826–836, https://doi.org/10.1007/s13351-019-9022-0.

- Chung, P.-H., and T. Li, 2013: Interdecadal relationship between the mean state and El Niño types. *J. Climate*, **26**, 361–379, https://doi.org/10.1175/JCLI-D-12-00106.1.
- Ciasto, L. M., G. R. Simpkins, and M. H. England, 2015: Teleconnections between tropical Pacific SST anomalies and extratropical Southern Hemisphere climate. *J. Climate*, **28**, 56–65, https://doi.org/10.1175/JCLI-D-14-00438.1.
- Clem, K. R., and R. L. Fogt, 2015: South Pacific circulation changes and their connection to the tropics and regional Antarctic warming in austral spring, 1979–2012. *J. Geophys. Res. Atmos.*, 120, 2773–2792, https://doi.org/10.1002/ 2014JD022940.
- —, and J. A. Renwick, 2015: Austral spring Southern Hemisphere circulation and temperature changes and links to the SPCZ. *J. Climate*, 28, 7371–7384, https://doi.org/10.1175/JCLI-D-15-0125.1.
- —, —, and J. McGregor, 2017: Large-scale forcing of the Amundsen Sea low and its influence on sea ice and West Antarctic temperature. *J. Climate*, 30, 8405–8424, https://doi.org/10.1175/JCLI-D-16-0891.1.
- —, B. R. Lintner, A. J. Broccoli, and J. R. Miller, 2019: Role of the South Pacific convergence zone in West Antarctic decadal climate variability. *Geophys. Res. Lett.*, 46, 6900–6909, https:// doi.org/10.1029/2019GL082108.
- Ding, Q. H., E. J. Steig, D. S. Battisti, and M. Küttel, 2011: Winter warming in West Antarctica caused by central tropical Pacific warming. *Nat. Geosci.*, 4, 398–403, https://doi.org/10.1038/ ngeo1129.
- —, —, and J. M. Wallace, 2012: Influence of the tropics on the southern annular mode. *J. Climate*, **25**, 6330–6348, https://doi.org/10.1175/JCLI-D-11-00523.1.
- Feng, J., W. Chen, C. Y. Tam, and W. Zhou, 2011: Different impacts of El Niño and El Niño Modoki on China rainfall in the decaying phases. *Int. J. Climatol.*, 31, 2091–2101, https://doi.org/10.1002/joc.2217.
- —, Y. Zhang, Q. Cheng, X. S. Liang, and T. Jiang, 2019: Analysis of summer Antarctic sea ice anomalies associated with the spring Indian Ocean Dipole. *Global Planet. Change*, 181, 102982, https://doi.org/10.1016/j.gloplacha.2019.102982.
- Harangozo, S. A., 2000: A search for ENSO teleconnections in the west Antarctic Peninsula climate in austral winter. *Int. J. Climatol.*, **20**, 663–679, https://doi.org/10.1002/(SICI)1097-0088(200005)20:6<663::AID-JOC493>3.0.CO;2-I.
- Held, I. M., and M. J. Suarez, 1994: A proposal for the intercomparison of the dynamical cores of atmospheric general circulation models. *Bull. Amer. Meteor. Soc.*, 75, 1825–1830, https://doi.org/10.1175/1520-0477(1994)075<1825:APFTIO> 2.0.CO;2.
- Henderson, S. A., E. D. Maloney, and E. A. Barnes, 2016: The influence of the Madden–Julian oscillation on Northern Hemisphere winter blocking. *J. Climate*, 29, 4597–4616, https://doi.org/10.1175/JCLI-D-15-0502.1.
- Hitchman, M. H., and M. J. Rogal, 2010: ENSO influences on Southern Hemisphere column ozone during the winter to spring transition. *J. Geophys. Res.*, 115, D20104, https:// doi.org/10.1029/2009JD012844.
- Hobbs, W. R., and M. N. Raphael, 2010: The Pacific zonal asymmetry and its influence on Southern Hemisphere sea ice variability. *Antarct. Sci.*, 22, 559–571, https://doi.org/10.1017/S0954102010000283.
- Holland, P. R., and R. Kwok, 2012: Wind-driven trends in Antarctic sea-ice drift. *Nat. Geosci.*, **5**, 872–875, https://doi.org/10.1038/ngeo1627.

- Hurwitz, M. M., P. A. Newman, L. D. Oman, and A. M. Molod, 2011: Response of the Antarctic stratosphere to two types of El Niño events. J. Atmos. Sci., 68, 812–822, https://doi.org/ 10.1175/2011JAS3606.1.
- Jiang, X., and T. Li, 2005: Reinitiation of the boreal summer intraseasonal oscillation in the tropical Indian Ocean. *J. Climate*, 18, 3777–3795, https://doi.org/10.1175/JCLI3516.1.
- Jin, D., and B. P. Kirtman, 2009: Why the Southern Hemisphere ENSO responses lead ENSO. J. Geophys. Res., 114, D23101, https://doi.org/10.1029/2009JD012657.
- Kalnay, E., and Coauthors, 1996: The NCEP/NCAR 40-Year Reanalysis Project. Bull. Amer. Meteor. Soc., 77, 437–471, https://doi.org/ 10.1175/1520-0477(1996)077<0437:TNYRP>2.0.CO;2.
- Kao, H. Y., and J. Y. Yu, 2009: Contrasting eastern-Pacific and central-Pacific types of ENSO. J. Climate, 22, 615–632, https:// doi.org/10.1175/2008JCL12309.1.
- Karoly, D. J., 1989: Southern Hemisphere circulation features associated with El Niño-Southern Oscillation events. J. Climate, 2, 1239–1252, https://doi.org/10.1175/1520-0442(1989)002<1239:SHCFAW>2.0.CO;2.
- —, and B. J. Hoskins, 1983: The steady, linear response of the stratosphere to tropospheric forcing. *Quart. J. Roy. Meteor. Soc.*, **109**, 455–478, https://doi.org/10.1002/qj.49710946103.
- Kreutz, K. J., P. A. Mayewski, I. I. Pittalwala, L. D. Meeker, M. S. Twickler, and S. I. Whitlow, 2000: Sea level pressure variability in the Amundsen Sea region inferred from a West Antarctic glaciochemical record. *J. Geophys. Res.*, 105, 4047–4059, https://doi.org/10.1029/1999JD901069.
- Kug, J.-S., F.-F. Jin, and S.-I. An, 2009: Two types of El Niño events: Cold tongue El Niño and warm pool El Niño. *J. Climate*, **22**, 1499–1515, https://doi.org/10.1175/2008JCLI2624.1.
- Lee, T., and Coauthors, 2010: Record warming in the South Pacific and western Antarctica associated with the strong central-Pacific El Niño in 2009–10. *Geophys. Res. Lett.*, **37**, L19704, https://doi.org/10.1029/2010GL044865.
- Li, C., J.-J. Luo, and S. Li, 2017: Impacts of different types of ENSO on the interannual seesaw between the Somali and the Maritime Continent cross-equatorial flows. *J. Climate*, 30, 2621–2638, https://doi.org/10.1175/JCLI-D-16-0521.1.
- Li, T., B. Wang, C. P. Chang, and Y. S. Zhang, 2003: A theory for the Indian Ocean dipole-zonal mode. *J. Atmos. Sci.*, **60**, 2119–2135, https://doi.org/10.1175/1520-0469(2003) 060<2119:ATFTIO>2.0.CO;2.
- Li, X., D. M. Holland, E. P. Gerber, and C. Yoo, 2014: Impacts of the north and tropical Atlantic Ocean on the Antarctic Peninsula and sea ice. *Nature*, 505, 538–542, https://doi.org/ 10.1038/nature12945.
- Liebmann, B., and C. A. Smith, 1996: Description of a complete (interpolated) outgoing longwave radiation dataset. *Bull. Amer. Meteor. Soc.*, 77, 1275–1277, https://doi.org/10.1175/1520-0477-77.6.1274.
- Liu, J. P., X. J. Yuan, D. Rind, and D. G. Martinson, 2002: Mechanism study of the ENSO and southern high latitude climate teleconnections. *Geophys. Res. Lett.*, 29, 1679, https:// doi.org/10.1029/2002GL015143.
- —, J. A. Curry, and D. G. Martinson, 2004: Interpretation of recent Antarctic sea ice variability. *Geophys. Res. Lett.*, 31, L02205, https://doi.org/10.1029/2003GL018732.
- Luo, J.-J., R. C. Zhang, S. K. Behera, Y. Masumoto, F.-F. Jin, R. Lukas, and T. Yamagata, 2010: Interaction between El Niño and extreme Indian Ocean dipole. *J. Climate*, 23, 726– 742, https://doi.org/10.1175/2009JCLI3104.1.

- —, W. Sasaki, and Y. Masumoto, 2012: Indian Ocean warming modulates Pacific climate change. *Proc. Natl. Acad. Sci. USA*, **109**, 18701–18706, https://doi.org/10.1073/ pnas.1210239109.
- Meehl, G. A., J. M. Arblaster, C. T. Y. Chung, M. M. Holland, A. DuVivier, L. Thompson, D. Yang, and C. M. Bitz, 2019: Sustained ocean changes contributed to sudden Antarctic sea ice retreat in late 2016. *Nat. Commun.*, 10, 14, https://doi.org/ 10.1038/s41467-018-07865-9.
- Mo, K. C., 2000: Relationships between low-frequency variability in the Southern Hemisphere and sea surface temperature anomalies. *J. Climate*, **13**, 3599–3610, https://doi.org/10.1175/1520-0442(2000)013<3599:RBLFVI>2.0.CO;2.
- Naveira Garabato, A. C., J. D. Zika, L. Jullion, P. J. Brown, P. R. Holland, M. P. Meredith, and S. Bacon, 2016: The thermodynamic balance of the Weddell Gyre. *Geophys. Res. Lett.*, 43, 317–325, https://doi.org/10.1002/2015GL066658.
- Nuncio, M., and X. Yuan, 2015: The influence of the Indian Ocean dipole on Antarctic sea ice. J. Climate, 28, 2682–2690, https:// doi.org/10.1175/JCLI-D-14-00390.1.
- Okumura, Y. M., 2019: ENSO diversity from an atmospheric perspective. *Curr. Climate Change Rep.*, **5**, 245–257, https://doi.org/10.1007/s40641-019-00138-7.
- —, D. Schneider, C. Deser, and R. Wilson, 2012: Decadal-interdecadal climate variability over Antarctica and linkages to the tropics: Analysis of ice core, instrumental, and tropical proxy data. *J. Climate*, 25, 7421–7441, https://doi.org/10.1175/JCLI-D-12-00050.1.
- Parkinson, C. L., 2019: A 40-y record reveals gradual Antarctic sea ice increases followed by decreases at rates far exceeding the rates seen in the Arctic. *Proc. Natl. Acad. Sci. USA*, 116, 14414–14423, https://doi.org/10.1073/pnas.1906556116.
- —, and D. J. Cavalieri, 2012: Antarctic sea ice variability and trends, 1979–2010. *Cryosphere*, 6, 871–880, https://doi.org/ 10.5194/tc-6-871-2012.
- Pellichero, V., J. B. Sallee, C. C. Chapman, and S. M. Downes, 2018: The Southern Ocean meridional overturning in the seaice sector is driven by freshwater fluxes. *Nat. Commun.*, 9, 1789, https://doi.org/10.1038/s41467-018-04101-2.
- Pezza, A. B., H. A. Rashid, and I. Simmonds, 2012: Climate links and recent extremes in Antarctic sea ice, high-latitude cyclones, Southern Annular Mode and ENSO. *Climate Dyn.*, 38, 57–73, https://doi.org/10.1007/s00382-011-1044-y.
- Purich, A., and M. H. England, 2019: Tropical teleconnections to Antarctic sea ice during austral spring 2016 in coupled pacemaker experiments. *Geophys. Res. Lett.*, **46**, 6848–6858, https://doi.org/10.1029/2019GL082671.
- Rayner, N. A., D. E. Parker, E. B. Horton, C. K. Folland, L. V. Alexander, D. P. Rowell, E. C. Kent, and A. Kaplan, 2003: Global analyses of sea surface temperature, sea ice, and night marine air temperature since the late nineteenth century. *J. Geophys. Res.*, 108, 4407, https://doi.org/10.1029/2002JD002670.
- Ren, H. L., and F. F. Jin, 2011: Niño indices for two types of ENSO. *Geophys. Res. Lett.*, 38, L04704, https://doi.org/ 10.1029/2010GL046031.
- Renwick, J. A., 2002: Southern Hemisphere circulation and relations with sea ice and sea surface temperature. *J. Climate*, **15**, 3058–3068, https://doi.org/10.1175/1520-0442(2002)015<3058: SHCARW>2.0.CO:2.
- Reynolds, R. W., N. A. Rayner, T. M. Smith, D. C. Stokes, and W. Q. Wang, 2002: An improved in situ and satellite SST analysis for climate. *J. Climate*, **15**, 1609–1625, https://doi.org/10.1175/1520-0442(2002)015<1609:AIISAS>2.0.CO;2.

- Rind, D., M. Chandler, J. Lerner, D. G. Martinson, and X. Yuan, 2001: Climate response to basin-specific changes in latitudinal temperature gradients and implications for sea ice variability. *J. Geophys. Res.*, 106, 20161–20173, https://doi.org/10.1029/ 2000JD900643.
- Rintoul, S. R., and Coauthors, 2018: Choosing the future of Antarctica. *Nature*, **558**, 233–241, https://doi.org/10.1038/ s41586-018-0173-4.
- Rondanelli, R., B. Hatchett, J. Rutllant, D. Bozkurt, and R. Garreaud, 2019: Strongest MJO on record triggers extreme Atacama rainfall and warmth in Antarctica. *Geophys. Res. Lett.*, 46, 3482–3491, https://doi.org/10.1029/2018GL081475.
- Saji, N. H., B. N. Goswami, P. N. Vinayachandran, and T. Yamagata, 1999: A dipole mode in the tropical Indian Ocean. *Nature*, 401, 360–363, https://doi.org/10.1038/43854.
- —, T. Ambrizzi, and S. E. T. Ferraz, 2005: Indian Ocean Dipole mode events and austral surface air temperature anomalies. *Dyn. Atmos. Oceans*, 39, 87–101, https://doi.org/10.1016/ j.dynatmoce.2004.10.015.
- Sardeshmukh, P. D., and B. J. Hoskins, 1988: The generation of global rotational flow by steady idealized tropical divergence. *J. Atmos. Sci.*, 45, 1228–1251, https://doi.org/10.1175/1520-0469(1988)045<1228:TGOGRF>2.0.CO;2.
- Schneider, D. P., and E. J. Steig, 2008: Ice cores record significant 1940s Antarctic warmth related to tropical climate variability. *Proc. Natl. Acad. Sci. USA*, 105, 12 154–12 158, https://doi.org/ 10.1073/pnas.0803627105.
- Scott, R. C., J. P. Nicolas, D. H. Bromwich, J. R. Norris, and D. Lubin, 2019: Meteorological drivers and large-scale climate forcing of West Antarctic surface melt. *J. Climate*, 32, 665–684, https://doi.org/10.1175/JCLI-D-18-0233.1.
- Simmonds, I., and X. Wu, 1993: Cyclone behaviour response to changes in winter Southern Hemisphere sea-ice concentration. *Quart. J. Roy. Meteor. Soc.*, 119, 1121–1148, https:// doi.org/10.1002/qj.49711951313.
- —, and T. H. Jacka, 1995: Relationships between the interannual variability of Antarctic sea ice and the Southern Oscillation. *J. Climate*, **8**, 637–647, https://doi.org/10.1175/1520-0442(1995) 008<0637:RBTIVO>2.0.CO;2.
- Simpkins, G. R., L. M. Ciasto, D. W. J. Thompson, and M. H. England, 2012: Seasonal relationships between large-scale climate variability and Antarctic sea ice concentration. *J. Climate*, 25, 5451–5469, https://doi.org/10.1175/JCLI-D-11-00367.1.
- Song, H.-J., E. Choi, G.-H. Lim, Y. H. Kim, J.-S. Kug, and S.-W. Yeh, 2011: The central Pacific as the export region of the El Niño–Southern Oscillation sea surface temperature anomaly to Antarctic sea ice. *J. Geophys. Res.*, 116, D21113, https://doi.org/10.1029/2011JD015645.
- Stammerjohn, S. E., D. G. Martinson, R. C. Smith, X. Yuan, and D. Rind, 2008: Trends in Antarctic annual sea ice retreat and advance and their relation to El Niño–Southern Oscillation and Southern Annular Mode variability. *J. Geophys. Res.*, 113, C03S90, https://doi.org/10.1029/2007JC004269.
- Steig, E. J., 2019: How fast will the Antarctic ice sheet retreat? Science, 364, 936–937, https://doi.org/10.1126/science.aax2626.
- Sun, D., F. Xue, and T. J. Zhou, 2013: Impacts of two types of El Niño atmospheric circulation in the Southern Hemisphere. Adv. Atmos. Sci., 30, 1732–1742, https://doi.org/10.1007/s00376-013-2287-9.
- Takaya, K., and H. Nakamura, 2001: A formulation of a phaseindependent wave-activity flux for stationary and migratory quasigeostrophic eddies on a zonally varying basic flow.

- *J. Atmos. Sci.*, **58**, 608–627, https://doi.org/10.1175/1520-0469(2001)058<0608:AFOAPI>2.0.CO:2.
- Timmermann, A., and Coauthors, 2018: El Niño-Southern Oscillation complexity. *Nature*, **559**, 535–545, https://doi.org/10.1038/s41586-018-0252-6.
- Ting, M. F., and L. H. Yu, 1998: Steady response to tropical heating in wavy linear and nonlinear baroclinic models. *J. Atmos. Sci.*, 55, 3565–3582, https://doi.org/10.1175/1520-0469(1998)055<3565:SRTTHI>2.0.CO:2.
- Turner, J., 2004: The El Niño-southern oscillation and Antarctica. *Int. J. Climatol.*, **24**, 1–31, https://doi.org/10.1002/joc.965.
- —, J. S. Hosking, G. J. Marshall, T. Phillips, and T. J. Bracegirdle, 2016: Antarctic sea ice increase consistent with intrinsic variability of the Amundsen Sea low. *Climate Dyn.*, 46, 2391–2402, https://doi.org/10.1007/s00382-015-2708-9.
- —, T. Phillips, G. J. Marshall, J. S. Hosking, J. O. Pope, T. J. Bracegirdle, and P. Deb, 2017: Unprecedented springtime retreat of Antarctic sea ice in 2016. *Geophys. Res. Lett.*, 44, 6868–6875, https://doi.org/10.1002/2017GL073656.
- Vernet, M., and Coauthors, 2019: The Weddell Gyre, Southern Ocean: Present knowledge and future challenges. *Rev. Geophys.*, 57, 623–708, https://doi.org/10.1029/2018RG000604.
- Wang, B., R. G. Wu, and T. Li, 2003: Atmosphere–warm ocean interaction and its impacts on Asian–Australian monsoon variation. *J. Climate*, **16**, 1195–1211, https://doi.org/10.1175/1520-0442(2003)16<1195:AOIAII>2.0.CO;2.
- Wang, G., H. H. Hendon, J. M. Arblaster, E.-P. Lim, S. Abhik, and P. van Rensch, 2019a: Compounding tropical and stratospheric forcing of the record low Antarctic sea-ice in 2016. *Nat. Commun.*, 10, 13, https://doi.org/10.1038/s41467-018-07689-7.
- Wang, L., T. Li, L. Chen, S. K. Behera, and T. Nasuno, 2018: Modulation of the MJO intensity over the equatorial western Pacific by two types of El Niño. *Climate Dyn.*, 51, 687–700, https://doi.org/10.1007/s00382-017-3949-6.
- Wang, Q., S. L. Li, J. J. Fu, and G. P. Li, 2012: Formation of the anomalous summer precipitation in east China in 2010 and 1998: A comparison of the impacts of two kinds of El Niño. *Acta Meteor. Sin.*, **26**, 665–682, https://doi.org/10.1007/s13351-012-0601-6.
- Wang, Z. M., J. Turner, Y. Wu, and C. Y. Liu, 2019b: Rapid decline of total Antarctic sea ice extent during 2014–16 controlled by wind-driven sea ice drift. J. Climate, 32, 5381–5395, https:// doi.org/10.1175/JCLI-D-18-0635.1.
- Wassermann, S., C. Schmitt, C. Kottmeier, and I. Simmonds, 2006: Coincident vortices in Antarctic wind fields and sea ice motion. *Geophys. Res. Lett.*, 33, L15810, https://doi.org/10.1029/2006GL026005.
- Webster, P. J., A. M. Moore, J. P. Loschnigg, and R. R. Leben, 1999: Coupled ocean–atmosphere dynamics in the Indian Ocean during 1997–98. *Nature*, 401, 356–360, https://doi.org/ 10.1038/43848.
- Welhouse, L. J., M. A. Lazzara, L. M. Keller, G. J. Tripoli, and M. H. Hitchman, 2016: Composite analysis of the effects of ENSO events on Antarctica. J. Climate, 29, 1797–1808, https:// doi.org/10.1175/JCLI-D-15-0108.1.
- White, W. B., and R. G. Peterson, 1996: An Antarctic circumpolar wave in surface pressure, wind, temperature and seaice extent. *Nature*, 380, 699–702, https://doi.org/10.1038/380699a0.
- Wilson, A. B., D. H. Bromwich, K. M. Hines, and S. H. Wang, 2014: El Niño flavors and their simulated impacts on atmospheric circulation in the high southern latitudes. *J. Climate*, 27, 8934– 8955, https://doi.org/10.1175/JCLI-D-14-00296.1.

- Wu, R., and J. L. Kinter III, 2010: Atmosphere–ocean relationship in the midlatitude North Pacific: Seasonal dependence and east–west contrast. J. Atmos. Sci., 115, D06101, https://doi.org/ 10.1029/2009JD012579.
- Xiang, B., B. Wang, and T. Li, 2013: A new paradigm for the predominance of standing central Pacific warming after the late 1990s. *Climate Dyn.*, 41, 327–340, https://doi.org/10.1007/ s00382-012-1427-8.
- Yeh, S.-W., J.-S. Kug, B. Dewitte, M.-H. Kwon, B. P. Kirtman, and F.-F. Jin, 2009: El Niño in a changing climate. *Nature*, **461**, 511–514, https://doi.org/10.1038/nature08316.
- Yu, J.-Y., and H.-Y. Kao, 2007: Decadal changes of ENSO persistence barrier in SST and ocean heat content indices: 1958–2001. J. Geophys. Res., 112, D13106, https://doi.org/10.1029/2006JD007654.
- —, H. Paek, E. S. Saltzman, and T. Lee, 2015: The early 1990s change in ENSO-PSA-SAM relationships and its impact on Southern Hemisphere climate. *J. Climate*, 28, 9393–9408, https://doi.org/10.1175/JCLI-D-15-0335.1.
- Yuan, X. J., 2004: ENSO-related impacts on Antarctic sea ice: A synthesis of phenomenon and mechanisms. *Antarct. Sci.*, 16, 415–425, https://doi.org/10.1017/S0954102004002238.

- —, and D. G. Martinson, 2000: Antarctic sea ice extent variability and its global connectivity. *J. Climate*, **13**, 1697–1717, https://doi.org/ 10.1175/1520-0442(2000)013<1697:ASIEVA>2.0.CO;2.
- —, and —, 2001: The Antarctic dipole and its predictability. Geophys. Res. Lett., 28, 3609–3612, https://doi.org/10.1029/2001GL012969.
- —, and C. H. Li, 2008: Climate modes in southern high latitudes and their impacts on Antarctic sea ice. *J. Geophys. Res.*, 113, C06S91, https://doi.org/10.1029/2006JC004067.
- —, M. R. Kaplan, and M. A. Cane, 2018: The interconnected global climate system—A review of tropical–polar teleconnections. *J. Climate*, 31, 5765–5792, https://doi.org/10.1175/JCLI-D-16-0637.1.
- Zhang, C., J.-J. Luo, and S. Li, 2019: Impacts of tropical Indian and Atlantic Ocean warming on the occurrence of the 2017/2018 La Niña. *Geophys. Res. Lett.*, 46, 3435–3445, https://doi.org/ 10.1029/2019GL082280.
- Zuo, H., M. A. Balmaseda, S. Tietsche, K. Mogensen, and M. Mayer, 2019: The ECMWF operational ensemble reanalysis–analysis system for ocean and sea ice: A description of the system and assessment. *Ocean Sci.*, 15, 779–808, https://doi.org/10.5194/os-15-779-2019.